J. Fluid Mech. (2013), *vol.* 721, *pp.* 86–117. © Cambridge University Press 2013
doi:10.1017/jfm.2013.41

Rapid gravitational adjustment of horizontal shear flows

Brian L. White[1],† **and Karl R. Helfrich**[2]

[1]Marine Sciences Department, UNC-Chapel Hill, NC 27599, USA
[2]Department of Physical Oceanography, Woods Hole Oceanographic Institution,
Woods Hole, MA 02543, USA

(Received 29 August 2011; revised 19 December 2012; accepted 16 January 2013)

The evolution of a horizontal shear layer in the presence of a horizontal density gradient is explored by three-dimensional numerical simulations. These flows exhibit characteristics of both free shear flows and gravity currents, but have complex dynamics due to strong interactions between the turbulent features of each. Vertical vortices produced by horizontal shear are tilted and stretched by the gravitational adjustment, rapidly enhancing vorticity. Shear intensification at frontal convergences produces high-wavenumber vertical vorticity and the slumping of the density interface produces horizontal Kelvin–Helmholtz vortices typical of a gravity current. The interaction between these instabilities promotes a rapid transition to three-dimensional turbulence. The flow development depends on the relative time scales of shear instability and gravitational adjustment, described by a parameter γ (where the limits $\gamma \rightarrow \infty$ and $\gamma \rightarrow 0$ represent a pure gravity current and a pure mixing layer, respectively). The growth rate of three-dimensional instability and the mixing increase for smaller γ. When γ is sufficiently small, there are two distinct regimes: an early period of during which the interface grows rapidly, followed by horizontal diffusive growth. Numerical results are consistent with field observations of tidal separation flows in the Haro Strait (Farmer, Pawlowicz & Jiang, *Dyn. Atmos. Oceans.*, vol. 36, 2002, pp. 43–58), including the magnitude of downwelling vertical currents, horizontal scales of surface vortex features and mixing rate.

Key words: gravity currents, shear layers, stratified flows

1. Introduction

The dynamics of stratified shear flows have received considerable attention due to their importance for ocean mixing and energy fluxes. Most work to date has focused on vertically sheared, vertically stratified flow, often with continuous stratification and shear (Shih *et al.* 2005; Ivey, Winters & Koseff 2008). In these cases, mixing is due to Kelvin–Helmholtz or Holmboe instabilities (Carpenter, Balmforth & Lawrence 2010), which are strongly damped by the stratification. The mixing depends on the strength of the stratification through the square of the buoyancy frequency, $N^2 = -(g/\rho_o)\,\mathrm{d}\rho/\mathrm{d}z$, and strength of the vertical shear, $\mathrm{d}u/\mathrm{d}z$. Here u is the horizontal velocity, ρ is the

---

† Email address for correspondence: bwhite@unc.edu

density, ρ_o is a reference density, g is the acceleration due to gravity and z is the vertical coordinate. Shear instability and mixing occur when the Richardson number, $Ri = N^2/(\mathrm{d}u/\mathrm{d}z)^2$, is below a critical value, generally $Ri_c = 0.25$. In contrast, the case in which horizontal shear couples with horizontal density stratification has been less studied, in part because it is unconditionally unstable: the horizontal density gradient leads to gravitational collapse, while horizontal shear is unstable to a Rayleigh shear instability. This configuration is common in the coastal ocean, and can be found in estuarine outflows, coastal fronts with along-front shear, island wakes and at the lateral edges of river plumes. The coupling between horizontal shear and density stratification has the potential to create mixing much more intense than that which occurs in a stably stratified vertical shear flow.

This work is motivated in part by observations of Farmer, Pawlowicz & Jiang (2002) of intense mixing in the flow downstream of Stuart Island in Haro Strait. The horizontal shear, that originates at the separation point between the stagnant lee of the island and the faster tidal flow, leads to the growth of vortices with vertically oriented axes through a classic Rayleigh shear instability. At the same time, because the water in the lee of Stuart Island is less dense than the tidal flow, there is a transverse baroclinic adjustment which, ignoring for the moment horizontal shear, is essentially a lock exchange, with time replaced by downstream distance using the mean velocity. As a result, the density front tilts under gravity downstream of the separation point. Observations suggest a particularly strong interaction between shear and baroclinic adjustment. Farmer *et al.* (2002) observed intense surface whirlpools and bubble plumes being pulled down from the surface to depths of over 100 m. They hypothesized that the baroclinic tilting stretches initially vertical Rayleigh vortices, intensifying their circulation while also converting vertical to horizontal vorticity.

The combination of enhanced vertical shear, lateral and vertical advection of density by the tilted vortices, and subsequent breakdown of the vortices was hypothesized to lead to the observed intense mixing. The shear layer evolution develops over only about 4 km in water of approximately 200 m depth, and over time scales of a few minutes for vortex roll-up, to less than an hour for the downstream advection and stretching phase. These are much shorter than the tidal or inertial periods, so the flow is essentially steady and unaffected by rotation. This problem bears some dynamical similarity to the horizontal baroclinic relaxation in the ocean mixed layer (Young 1994; Boccaletti, Ferrari & Fox-Kemper 2007), but in that problem the influence of rotation is much greater because time scales are much longer.

Basak & Sarkar (2006) studied the evolution of a horizontal shear layer superimposed upon a vertical density gradient. Although initially uniform in the horizontal, the density field develops horizontal gradients as a consequence of the shear instability. The vertical vortex cores associated with the horizontal shear became dislocated in the vertical by lateral density intrusions, creating a lattice of vortex cores connected by intrusions. This complexity lead to very thin sheets of high vertical shear and density gradient, and ultimately to enhanced mixing. Note that in this case the horizontal density adjustment is second-order compared with the horizontal shear, whereas in the situation considered here, the fluid is initially strongly stratified in the horizontal direction and the baroclinic collapse creates a transient flow with a highly non-equilibrium, secular evolution. Finally, we note that Boulanger, Meunier & Dizès (2008) studied the tilting of a stratified vortex and identified a shear-induced instability that occurred at a critical radius of the tilted vortex. The instability creates a zig-zag pattern of vortices, whose evolution is local and confined to a region of critical shear.

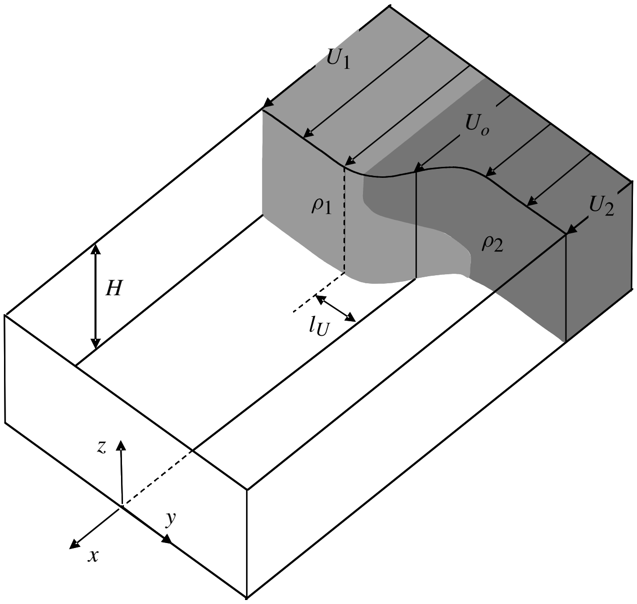

FIGURE 1. Schematic illustration of the shear flow problem. For all results presented here, $U_1 = -U_2 > 0$, $U_o = 0$ and $\rho_1 > \rho_2$. The displacement of the density interface shown in the figure is for illustrative purposes only.

For simplicity, we conceptualize the horizontal shear flow problem as a mixing layer that separates water masses of two different densities (see figure 1). Two vertically uniform, coflowing streams, one with speed U_1 and density ρ_1 and the other with speed U_2 and density ρ_2, are joined at a central transition zone. The resulting shear flow is modelled using a hyperbolic tangent,

$$u(y) = U_o + \frac{1}{2}\Delta U \tanh\left(\frac{y}{l_u}\right), \tag{1.1}$$

where $U_o = (U_1 + U_2)/2$ is the mean velocity, $\Delta U = U_2 - U_1$ is the velocity difference and l_u is the length scale for the horizontal shear. Similarly, the horizontal density profile is given by

$$\rho(y) = \rho_2 + \frac{1}{2}\Delta\rho\left[1 - \tanh\left(\frac{y}{l_\rho}\right)\right], \tag{1.2}$$

where $\Delta\rho = \rho_1 - \rho_2$ and l_ρ is the length scale for the density transition. Here we assume $\rho_1 > \rho_2$ and take the reference density $\rho_o = \rho_2$.

It is well known that an inviscid, homogeneous ($\Delta\rho = 0$), parallel shear flow is unstable, producing vortices that grow downstream, entraining irrotational fluid into the mixing layer and enhancing lateral mixing. The initial growth is by an inviscid instability and linear theory predicts the unstable modes and their growth rates. Michalke (1964) analysed the temporal growth of spatially periodic disturbances with the profile (1.1) and found that the most unstable wave was $kl_u = 0.445$, where k is the real wavenumber. The corresponding growth rate $kc_i = 0.095|\Delta U|/l_u$, where $c = c_r + \mathrm{i}c_i$ is the complex phase speed and $c_r = U_o$.

Numerous theoretical, numerical and experimental studies have shown the nonlinear evolution consists first of the two-dimensional vortex formation, followed by vortex pairing by a subharmonic instability (Pierrehumbert & Widnall 1982), and finally the development of a three-dimensional instability which causes the two-dimensional vortex tubes to break up into three-dimensional turbulence (Corcos & Lin 1984; Lasheras & Choi 1988). Even in the turbulent regime, vortices with coherent vertical vorticity are still observed (Brown & Roshko 1974), and lateral growth continues, predominantly by vortex pairing (Winant & Browand 1974).

The transverse gravitational collapse can be interpreted to first order as a lock-exchange gravity current (Simpson 1999). In the initial phase of collapse (without influence from boundaries), a gravity current front moves at a speed $c_f = (g'H)^{1/2}/2$, where $g' = (\Delta\rho/\rho_o)g$ is the reduced gravity (Benjamin 1968). Gravity currents are unstable to Kelvin–Helmholtz vortices oriented horizontally along the major axis of shear, which lead to turbulent mixing (Hartel, Meiburg & Necker 2000*b*). In the coupled shear flow–gravity current problem, the large-scale horizontal shear can be expected to modify the gravity current front speed and the development and evolution of Kelvin–Helmholtz instabilities.

The related problem of a gravity current subjected to strong mixing was considered by Linden & Simpson (1986). They artificially induced mixing by introducing bubbles into a lock exchange flow. They found that the flow initially evolves as an ideal gravity current, with a sharp front moving at constant speed and a balance between baroclinic pressure gradient and inertia. However, once the vertical mixing becomes significant, the fronts and interface between the layers become diffuse, reducing the horizontal pressure gradient and slowing the propagation speed.

The objective of this paper is to describe the dynamics of horizontal shear flows with a horizontal density gradient, using three-dimensional, variable-density, Navier–Stokes simulations. Particular attention is devoted to the front propagation, energetics, and mixing. The structure of the paper is as follows. In § 2, scaling arguments are used to derive a governing parameter that characterizes the two competing dynamical processes, horizontal shear and lateral gravitational adjustment. The numerical model and set-up of the problem are introduced in § 3. In § 4 we show results from the simulations for different values of the scaling parameter and describe the development and interaction of instabilities that develop and lead to intense mixing. In § 5 evolution of mean velocity and density fields are studied. Energy budgets are considered in § 6 and the mixing characteristics of these flows are discussed in § 7.

2. Scaling for shear layers with a horizontal density gradient

The interaction between a vortex arising from the instability of horizontal velocity shear and gravitational adjustment from the horizontal density difference results in a highly three-dimensional flow. In contrast to a homogeneous or vertically stratified shear flow, a linear instability analysis in the traditional sense is not appropriate because the base flow, $u(y)$, $\rho(y)$, results in an unbalanced horizontal pressure gradient, which produces a secular term in the linearized normal mode decomposition. Instead, some guidance about the development can found from the ratio of time scales for shear and gravitational adjustment. Recall that time and space scales of interest are such that rotation is generally not important. Neither are variations in the basic shear flow due to the tidal cycle, so that the free stream velocities $U_{1,2}$ and densities $\rho_{1,2}$ can be considered constant.

For the idealized parallel shear flow the most unstable wavenumber is $k \approx 0.45/l_u$ (Michalke 1964). The corresponding growth rate $kc_i \approx 0.1|\Delta U|/l_u$ gives a time scale for the emergence of vertical vortices from the shear instability,

$$\tau_s = (kc_i)^{-1} \approx \frac{10 l_u}{|\Delta U|}. \tag{2.1}$$

In the absence of shear, the horizontal density difference illustrated in figure 1 will produce a lock-exchange flow. After some initial adjustment, gravity currents will propagate at a speed $c_f \approx (g'H)^{1/2}/2$ in both directions away from the initial position of the front (Benjamin 1968). The time for the nose of the gravity current to move a distance L from the lock gives the gravity current time scale

$$\tau_{gc} = \frac{2L}{(g'H)^{1/2}}. \tag{2.2}$$

If the length scale L is taken to be the water depth H, then this time scale corresponds roughly to a factor of two stretching of the interface between the two fluids.

The competition between the shear instability and the gravitational adjustment (with $L = H$) is characterized by the ratio

$$\gamma = \frac{\tau_s}{\tau_{gc}} = 5 \frac{l_u}{H} \frac{(g'H)^{1/2}}{|\Delta U|}. \tag{2.3}$$

In the limit $\gamma \to \infty$, the flow is dominated by the gravity current which spreads horizontally before the shear instability has a chance to grow. The ensuing evolution will probably be only weakly affected by the horizontal shear and it seems unlikely that the classic horizontal shear instability will emerge since the basic state flow changes so rapidly. When $\gamma \to 0$, the shear instability can grow before the gravitational adjustment has time to occur and, at least initially, the density field should behave as a passive tracer. Gravitational adjustment will occur on a longer time scale and probably modify the vertical vortex. When $\gamma = O(1)$ both the shear instability and the gravitational instability evolve on the same time scale.

The parameter γ is also related to a horizontal Richardson number, which could be defined as

$$Ri_h = \frac{g}{\rho_o} \frac{\partial \rho / \partial x}{(\partial u / \partial x)^2} \sim \frac{g'H}{\Delta U^2} \left(\frac{l_u}{H}\right)^2 \left(\frac{H}{l_\rho}\right) = \left(\frac{\gamma^2}{25}\right) \left(\frac{H}{l_\rho}\right). \tag{2.4}$$

This is similar to the horizontal Richardson number defined for estuaries (Monismith *et al.* 2002) that compares the ratio of horizontal baroclinic forcing to vertical turbulent shear generated by bottom friction.

3. Numerical simulations

We have performed numerical simulations of the three-dimensional Boussinesq equations,

$$\frac{\mathrm{D}\boldsymbol{u}}{\mathrm{D}t} = -\nabla \Phi - s\hat{\boldsymbol{k}}, \quad \nabla \cdot \boldsymbol{u} = 0, \quad \frac{\mathrm{D}s}{\mathrm{D}t} = 0, \tag{3.1}$$

where $\Phi = p/\rho_o + gz$ is a potential given by the difference between the pressure, p, and its mean hydrostatic component and scaled by ρ_o, a constant reference density, $s = g(\rho - \rho_o)/\rho_o$ is the buoyancy and $\hat{\boldsymbol{k}}$ is the unit vector in the positive z-direction. The numerical domain for all calculations was a box of depth H, length L_x in the direction of the initial flow and width $2L_y$. The domain is periodic in the x-direction with free-slip boundaries in y and z. The velocity was initialized with a hyperbolic tangent profile (1.1) with $U_1 > 0$, $U_2 = -U_1 < 0$, so that $U_o = 0$,

$$u(y) = \frac{1}{2}\Delta U \tanh\left(\frac{y - y_p(x)}{l_u}\right), \tag{3.2}$$

and $v = w = 0$. Here $y_p(x) = 0.02\sin(2\pi x/L_x)$ is a small perturbation to the interface position with a wavelength equal to L_x, close to the most unstable wavelength. The initial density field is given by (1.2) with the perturbation $y_p(x)$,

$$\rho(y) = \rho_2 + \frac{\Delta\rho}{2}\left[1 - \tanh\left(\frac{y - y_p(x)}{l_\rho}\right)\right]. \tag{3.3}$$

Thus, both the initial velocity and density fields are independent of z. In addition to γ, the ratio l_ρ/l_u may influence the dynamics, particularly for $l_\rho/l_u \gg 1$, but we expect its effects to be secondary when $l_\rho/l_u \leqslant O(1)$. All simulations reported here use $l_u = l_\rho$.

In all simulations, we take $\rho_o \equiv \rho_2$, and scale all velocities by $(g'H)^{1/2}$, all lengths by H and time by $(H/g')^{1/2}$. From here forward, all variables are non-dimensional unless specifically stated. In non-dimensional variables $\gamma = 5l_u|\Delta U|^{-1}$.

For most simulations we use $l_u = l_\rho = 1/6$ (in addition to some runs with $l_u = l_\rho = 1/12$, which we discuss separately in §§ 6.1 and 7). The velocity and density transition thicknesses are small compared with the water depth, in qualitative agreement with the observations of Farmer *et al.* (2002). The domain has length $L_x = 2.6$ in x. The most unstable wavelength for the Rayleigh instability is $L_x = 2.33$. However, the growth rate for a disturbance with wavelength $L_x = 2.6$ is only 1 % smaller than the maximum. The transverse, y, length, $2L_y = 10.4$, is sufficient to keep the end walls from influencing either the shear instability (Huerre 1983) or the early stages of the gravity current propagation. The scaled total depth $H = 1$.

The evolution of the flow was followed with the three-dimensional, non-hydrostatic, adaptive-mesh model IAMR (Almgren *et al.* 1998) (see Lawrence Berkeley Laboratory CCSE software suite, http://seesar.lbl.gov/ccse). The model solves the Navier–Stokes equations on a Cartesian grid via a time-centred, second-order projection method with a Godunov scheme for the advective terms. It is well suited for these flows with large density and velocity gradients. Most simulations used a fixed resolution of 256 × 1024 × 128 in x, y and z, respectively (adaptive-mesh refinement was turned off). Simulations were also performed with a lower resolution of 192 × 768 × 96. The large-scale behaviour and energetics were very similar between the resolutions, but finer details were observed in the higher-resolution results, so only these results are discussed here. The code was run in a Boussinesq mode with viscosity and buoyancy diffusion coefficients set to zero. It has been demonstrated that high-order, non-oscillatory, finite-volume codes such as IAMR can accurately capture the energy cascade from the resolved dynamical scales to the dissipation range because the flux-conservative form casts the subgrid stress in the same form as a viscous stress tensor (Margolin, Smolarkiewicz & Wyszogradzki 2006; Aspden *et al.* 2008). This is known as implicit large eddy simulation (ILES). In a viscous flow, the dissipation scale is set by the Kolmogorov microscale, $\eta = \nu^{3/4}/\varepsilon_v^{1/4}$ where ν is the kinematic viscosity and ε_v is the kinetic energy dissipation rate. In ILES, energy is dissipated instead at the grid scale, Δx. For a viscous fluid the total dissipation in a closed volume is given by $\varepsilon_v = \nu\mathscr{D}$ where $\mathscr{D} = \int_V \boldsymbol{u} \cdot \nabla^2\boldsymbol{u}\,\mathrm{d}V$, so that the Kolmogorov scale can be recast as $\eta = \varepsilon_v^{1/2}/\mathscr{D}^{3/4}$. Analogously, one can define for ILES an effective Kolmogorov scale, $\eta_e = \varepsilon_v^{1/2}/\mathscr{D}^{3/4}$, where the numerical dissipation, ε_v, is calculated from the

γ	U	l_ρ	l_u	Rey_e	Scheme
1.67	0.5	1/6	1/6	16 828	ILES
0.83	1	1/6	1/6	9849	ILES
0.42	2	1/6	1/6	7015	ILES
0.21	4	1/6	1/6	3608	ILES
0.10	8	1/6	1/6	2306	ILES
1.67	0.25	1/12	1/12	14 251	ILES
0.83	0.5	1/12	1/12	10 978	ILES
0.42	1	1/12	1/12	8430	ILES
0.21	2	1/12	1/12	6298	ILES
0.10	4	1/12	1/12	7673	ILES
0.05	8	1/12	1/12	5856	ILES
0.42	2	1/6	1/6	4000	DNS

TABLE 1. Summary of numerical simulations.

residual of the kinetic energy budget. Similarly, an effective viscosity, $\nu_e = \varepsilon_v/\mathscr{D}$, and an effective Reynolds number, $Re_e = 1/\nu_e$, can also be defined. Note that the interpretation of effective viscosity does not imply that an ILES and direct numerical simulation (DNS) at the same effective Reynolds number will be identical, but the energetic cascades should behave very similarly.

Aspden *et al.* (2008) found for a homogenous turbulent flow that $\eta_e \sim \Delta x$ with a nearly constant proportionality constant, demonstrating an explicit link between the grid dissipation and viscosity. However, the translation to stratified fluids is less certain, as ILES models appear to be less studied for such flows. Small-scale behaviour, such as anisotropy in the dissipation, may create differences when ILES is applied to stratified fluids and the method implies that the Prandtl, or Schmidt, number is one. However, ILES was used successfully in several studies of turbulent, stratified flows. Lawrie & Dalziel (2011*a*,*b*) modelled the development of a Rayleigh–Taylor instability and found good agreement between experiments and their ILES simulations. Waite & Smolarkiewicz (2008) studied the breakdown and subsequent turbulent evolution of counter-rotating vertical vortices in a stratified system and found good agreement between ILES simulations and those from both a spectral-transform model with hyperviscosity and an explicit large eddy simulation (LES) model. In a study of thermal convection Piotrowski *et al.* (2009) found that ILES performed better than similarly resolved LES. So while there are certainly caveats to using an ILES model, there is evidence that reliable results can be obtained for stratified flows under a variety of conditions.

As a baseline, we have compared ILES with a DNS for the $\gamma = 0.42$ case and these results are discussed in § 8. We find that the turbulent spectra for each method agree very closely well into the dissipation range. This gives us confidence in the reliability of ILES for these flows and we use the method for the remainder of the runs. In all, six high-resolution runs were made spanning $\gamma = 0.1$ to ∞ ($\Delta U = 8$ to 0) and six additional runs were performed with the same ΔU, but with $l_u = 1/12$. A summary of all runs is given in table 1. Note that for the DNS run, the Reynolds number (4000) is based on explicit viscosity and the Prandtl number, $Pr = \nu/\kappa = 1$, where κ is the scalar diffusivity. For ILES runs, the Reynolds number is the average of the effective value, Re_e over the duration of the run.

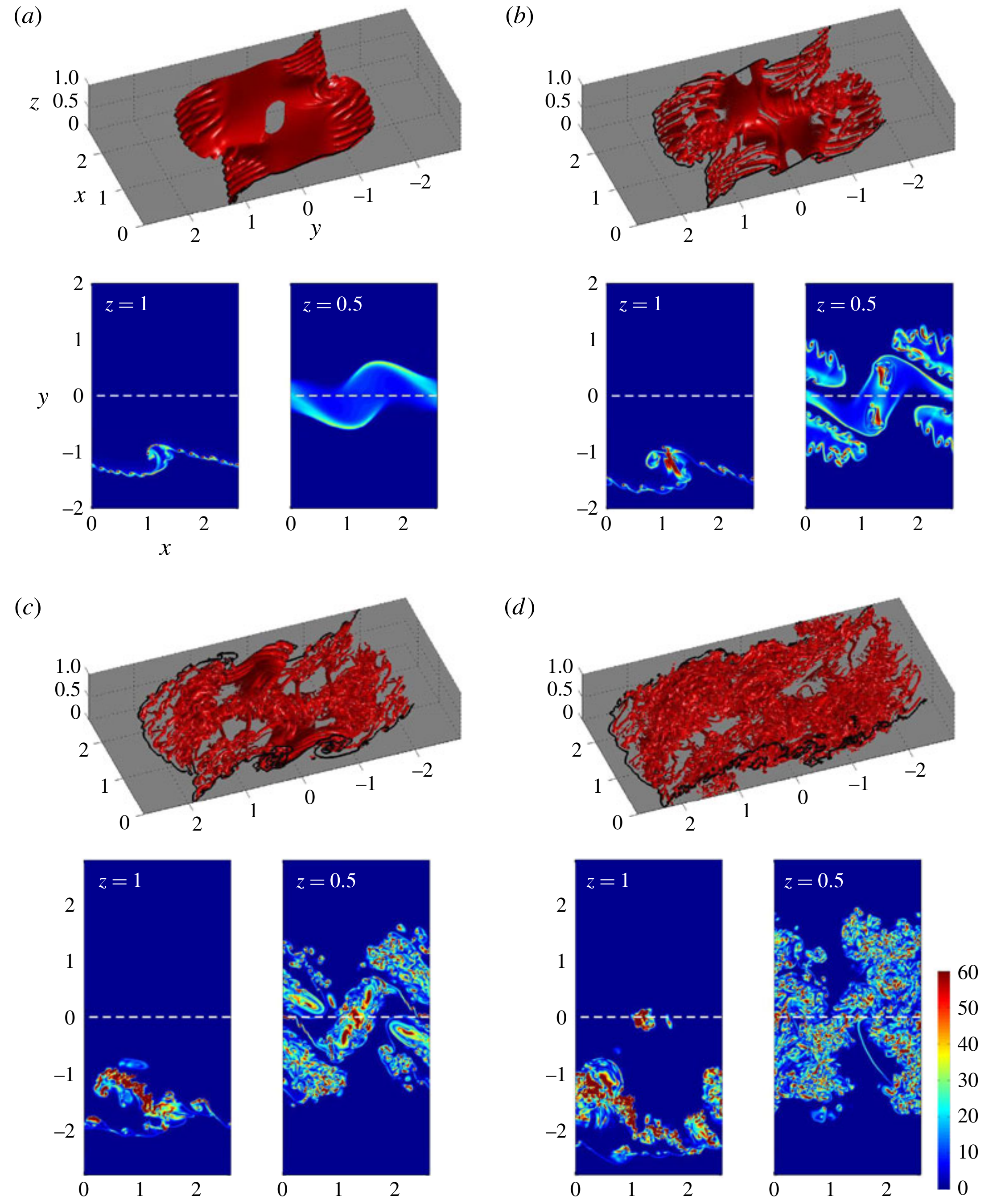

FIGURE 2. Vorticity structure for $\gamma = 0.42$ at the indicated times. (*a,b*) Isosurface of the vorticity magnitude, $|\omega|$: (*a*) $|\omega| = 15$; (*b*) $|\omega| = 30$. (*c,d*) Surface ($z = 1$) and mid-plane ($z = 0.5$) sections of $|\omega| = 30$. The $s = 0.5$ isocontour is shown in heavy black for reference: (*a*) $t = 2.75$; (*b*) $t = 3.25$; (*c*) $t = 4$; and (*d*) $t = 5$.

4. Flow development

4.1. *Evolution of the shear flow*

The numerical solutions for $\gamma = 0.42$ is presented in figure 2. The figures shows a three-dimensional isosurface and x–y plan view of the surface ($z = 1$) and mid-plane ($z = 0.5$) magnitude of the vorticity, $|\omega|$, at four times during evolution. The $z = 0$ plane (not shown) is a mirror image of the surface, due to the vertical symmetry properties of the Boussinesq solution. The initial maximum magnitude of the (non-dimensional) vertical vorticity in the horizontal shear layer $\omega_o = \Delta U/2l_u = 6$. Almost immediately, the vortex sheet begins to tilt due to gravitational adjustment. Simultaneously, the tilting sheet rolls up into a vertical vortex that by $t = 2.75$ has separated into two distinct cores. One is at the top, $z = 1$, and one at the bottom, $z = 0$. They are dislocated in y and slightly in x.

The propagation of the gravity current flow in the y-direction produces convergence along the surface and bottom fronts that thins the density interface and intensifies across-front shear. By $t = 2.75$ and 3.25, the vorticity magnitude $|\omega| \approx 60$ at $z = 1$, nearly 10 times the initial vorticity. This shear enhancement leads to a secondary shear instability and small vertical vortices along the both the $z = 0$ and $z = 1$ fronts. At least 12 of these secondary vortex cores are evident at $z = 1$ at $t = 2.75$. The velocity jump ΔU remains approximately constant across front, thus the increased vorticity is due to a thinning of the interface, or a decrease in l_u by roughly a factor of 10. From the classical shear layer results discussed earlier, the most unstable wavelength of the secondary shear instability should scale as $k^{-1} \sim l_u$, which explains the order of magnitude increase in the number of vertical vortices along the front. These secondary vortices appear as ripples in the vortex sheet along the top and bottom fronts. They are similar in appearance to the lobe-and-cleft instability seen in gravity currents along a no-slip boundary (Hartel, Carlsson & Thunblom 2000*a*). However, we emphasize that the boundaries in our simulations are free-slip, and the secondary instability is caused by a very different mechanism.

A third instability begins to form by $t = 3.25$ as Kelvin–Helmholtz rolls associated with the lateral gravity current appear. These are initially oriented in the horizontal plane (streamwise vorticity), approximately perpendicular to the primary vertical vortex cores. This orientation is evident from the mid-plane, $z = 0.5$, vorticity field at $t = 3.25$ (figure 2*b*). The rolls are aligned with the primary axes of strain associated with the horizontal shear. The secondary shear vortices associated with the frontal convergence are distributed along the Kelvin–Helmholtz rolls. The two dislocated primary vortex cores and the initial vortex sheet are still identifiable. The Kelvin–Helmholtz rolls parallel to the vorticity sheet form very sharp alternating fronts, separating high- and low-vorticity fluid.

The vorticity isosurface at $t = 3.25$ illustrates the skeleton of the emerging flow. The central region is formed by the two primarily dislocated and tilted vertical cores, around which are wrapped the Kelvin–Helmholtz vortices. Near the top and bottom, ribs have developed from the secondary shear instability on the converging fronts and are wound around the Kelvin–Helmholtz vortices. The development and interaction of the three instabilities leads to rapid breakdown of the flow into turbulence by $t = 4$ (figure 2*c*). The primary vertical vortices and the Kelvin–Helmholtz vortices are still apparent, but the vorticity has become highly convoluted and the ribbed structure has begun to disappear as the turbulence intensifies. Very large velocity gradients produce regions of very high vorticity, as seen in the surface and mid-plane vorticity contour plots (figure 2*c*). The alignment of the primary axes of shear and the Kelvin–Helmholtz billows are still evident in the mid-plane buoyancy plot. By $t = 5$ (figure 2*d*) the vorticity field has lost most of its structure, but the lateral adjustment continues as a highly turbulent gravity current.

The evolution for $\gamma = 0.21$, with twice the initial shear ($\omega_o = 12$), is shown in figure 3. The development is similar to $\gamma = 0.42$, but the primary horizontal shear

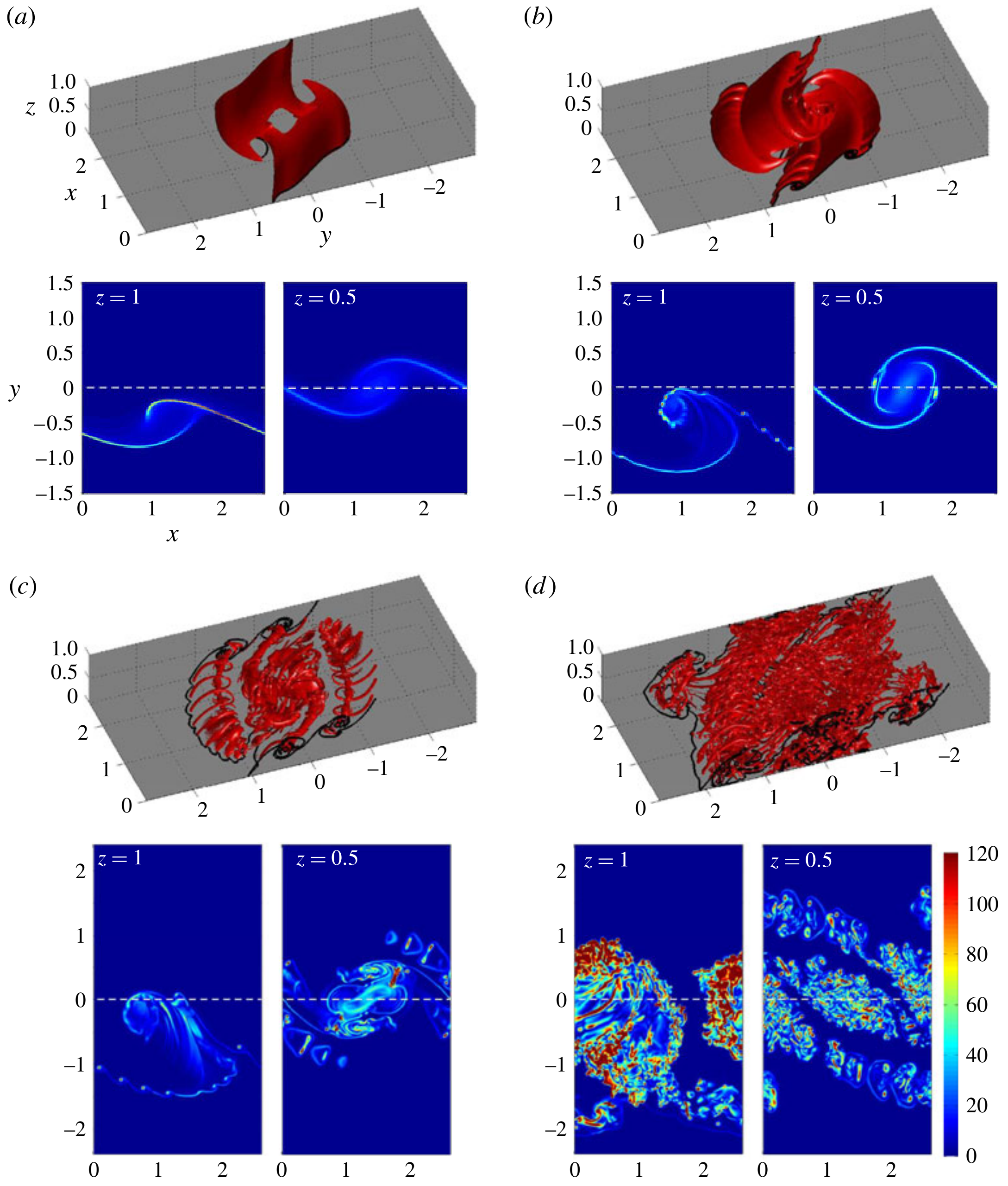

FIGURE 3. The same as figure 2 except $\gamma = 0.21$: (*a*) $t = 1.5$; (*b*) $t = 2$; (*c*) $t = 2.5$; and (*d*) $t = 3.5$. Isosurface $|\omega| = 18$ in (*a*) and (*b*) and $|\omega| = 42$ in (*c*) and (*d*).

instability develops more rapidly compared with the gravitational adjustment. While the primary shear roll-up occurs first, the Kelvin–Helmholtz vortices develop on a similar time scale as shown in figure 3(*b*). The secondary shear instability again emerges along the fronts. By $t = 2.5$ (figure 3*c*) a vorticity skeleton of ribs formed by the secondary shear vortices is wound around the Kelvin–Helmholtz billows. The primary vertical vortex is more concentrated along $y = 0$ and shows less evidence of dislocation in y. Coherent Kelvin–Helmholtz billows are wound around the central core. By $t = 3.5$ the flow becomes highly turbulent and nearly all structure breaks

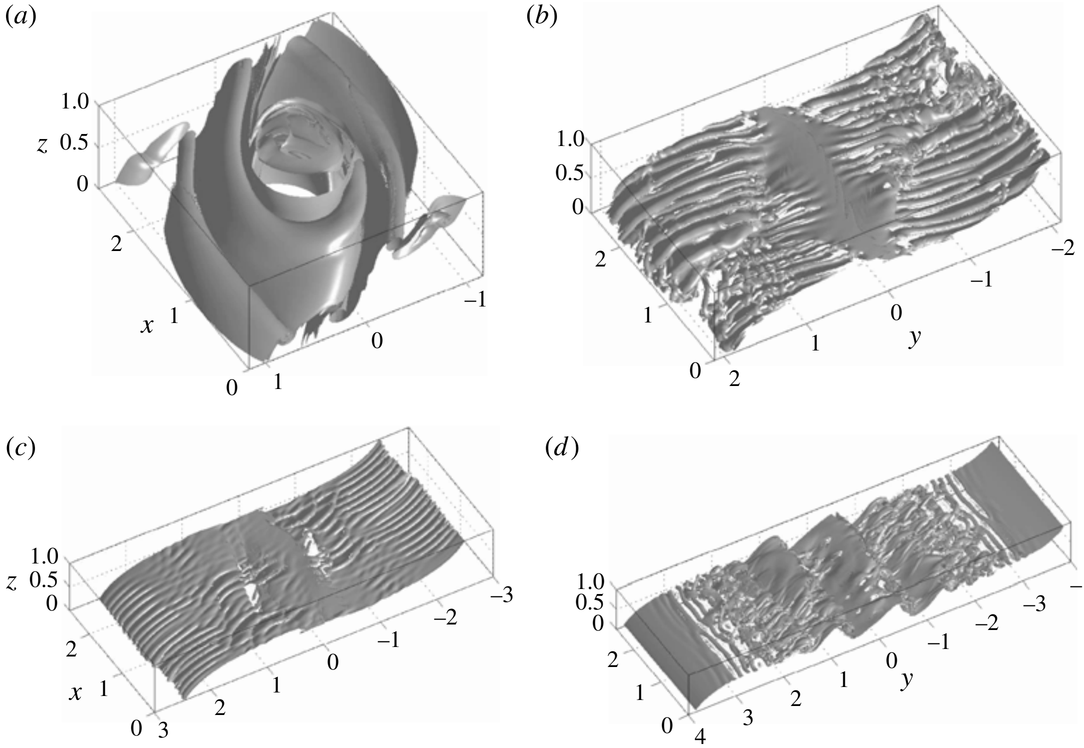

FIGURE 4. Isosurfaces of $|\omega|$ for other γ: (*a*) $\gamma = 0.1$, $t = 1.5$, $|\omega| = 15$; (*b*) $\gamma = 0.83$, $t = 4.25$, $|\omega| = 18$; (*c*) $\gamma = 1.67$, $t = 5.25$, $|\omega| = 15$; (*d*) $\gamma \to \infty$, $t = 8$, $|\omega| = 12$. Note that the *y*-axis limits are different for each case.

down. However, the mid-plane vorticity fields show the alignment of the vorticity fields along the primary axes of strain and a banded structure marking the central vortex core and the remnants of the Kelvin–Helmholtz billows.

Vorticity isosurface plots for $\gamma = 0.1, 0.83, 1.67$ and ∞ are shown in figure 4. Each case is shown at a different time since the flows evolve over different time scales. The smaller γ, the more rapid the turbulent breakdown. There is a transition from a flow dominated by the horizontal shear layer as $\gamma \to 0$ to a pure gravity current as $\gamma \to \infty$. The $\gamma = 0.83$ and 1.67 cases, like the $\gamma = 0.42$ and 0.21 runs in figures 2 and 3, show strong interactions between the shear instability and gravitational collapse, and the appearance of the secondary shear instability vortices along the surface and bottom fronts. As γ increases from 0.21 to 1.67 the secondary frontal instabilities progressively emerge sooner than the Kelvin–Helmholtz instability associated with the transverse gravitational adjustment. In contrast, the pure gravity current ($\gamma \to \infty$, figure 4*d*) only develops Kelvin–Helmholtz instabilities along the central, horizontal portion of the interface, while the fronts remain smooth. This is an important point because it illustrates that the secondary instabilities do not occur in the absence of along-front shear. However, based on the $\gamma = 1.67$ case, it appears that only a small amount shear is required for instabilities to develop. It is also important to note that these secondary instabilities begin at the fronts and move toward the centre, in contrast to the Kelvin–Helmholtz instabilities seen in the pure gravity current, which are confined to the centre, away from the fronts.

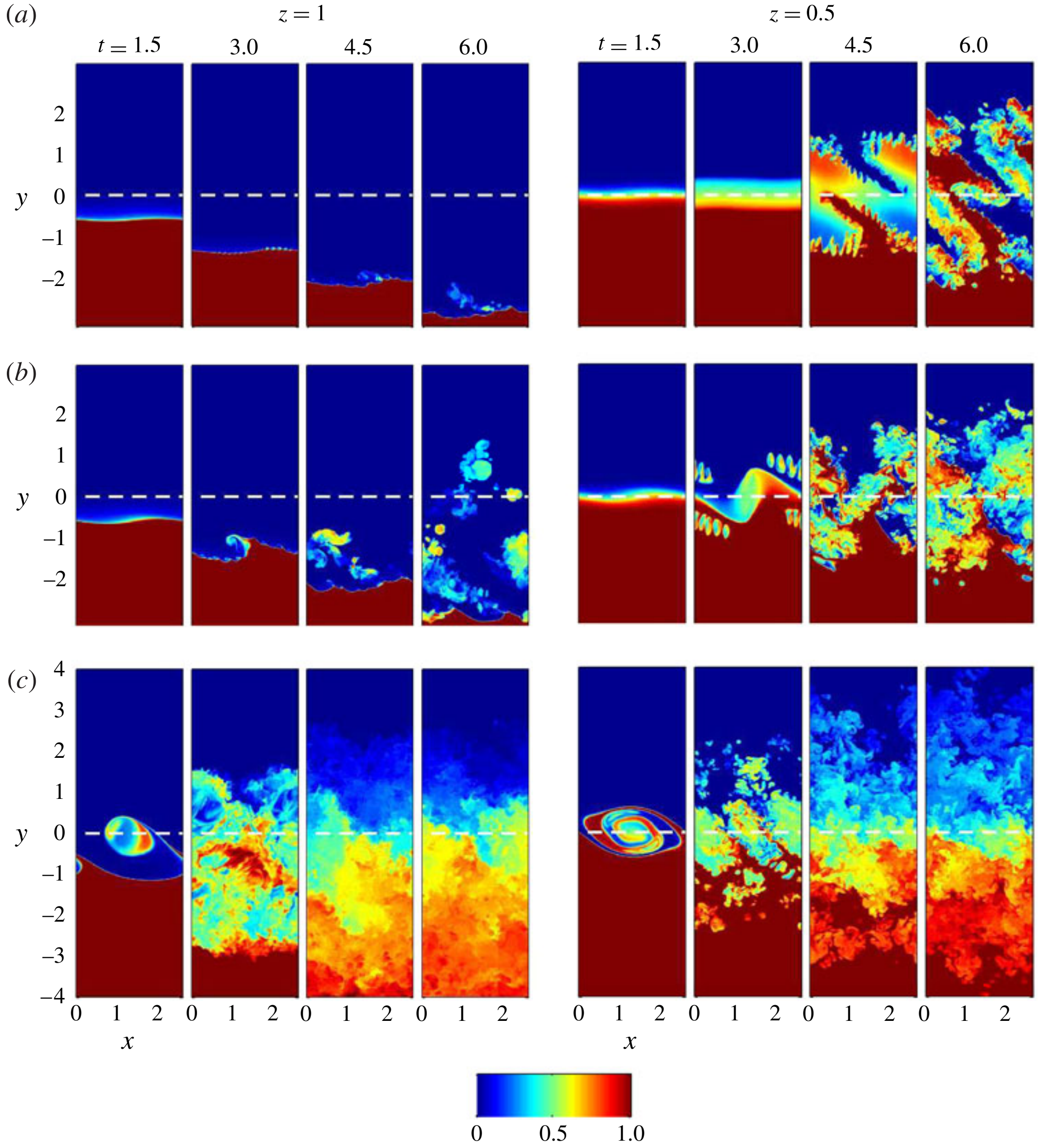

FIGURE 5. Surface ($z = 1$) and mid-plane ($z = 0.5$) buoyancy, s, fields at the indicated times: (*a*) $\gamma = 0.83$; (*b*) $\gamma = 0.42$; (*c*) $\gamma = 0.10$.

4.2. *Evolution of the buoyancy field*

Surface and mid-depth buoyancy fields at four evenly spaced times are shown in figure 5(*a*–*c*) for $\gamma = 0.83$, 0.42 and 0.1, respectively. The surface plots show that the front propagation resembles a gravity current for weak shear. The primary shear instability and the mixing increase as γ is decreased (increasing shear). For $\gamma = 0.1$ (figure 5*c*), the surface buoyancy field is so highly convoluted by $t = 3$ that the primary shear vortex is no longer recognizable. The intense convective overturning associated with the instabilities has brought dense fluid to the surface. Similar vigorous overturning occurs at $\gamma = 0.42$ for $t > 3$ (figure 5*b*).

To illustrate the source of the convective overturning, a sequence of buoyancy fields in a y–z section at $x = 0.96$ are shown in figure 6 for $\gamma = 0.21$. The figures also

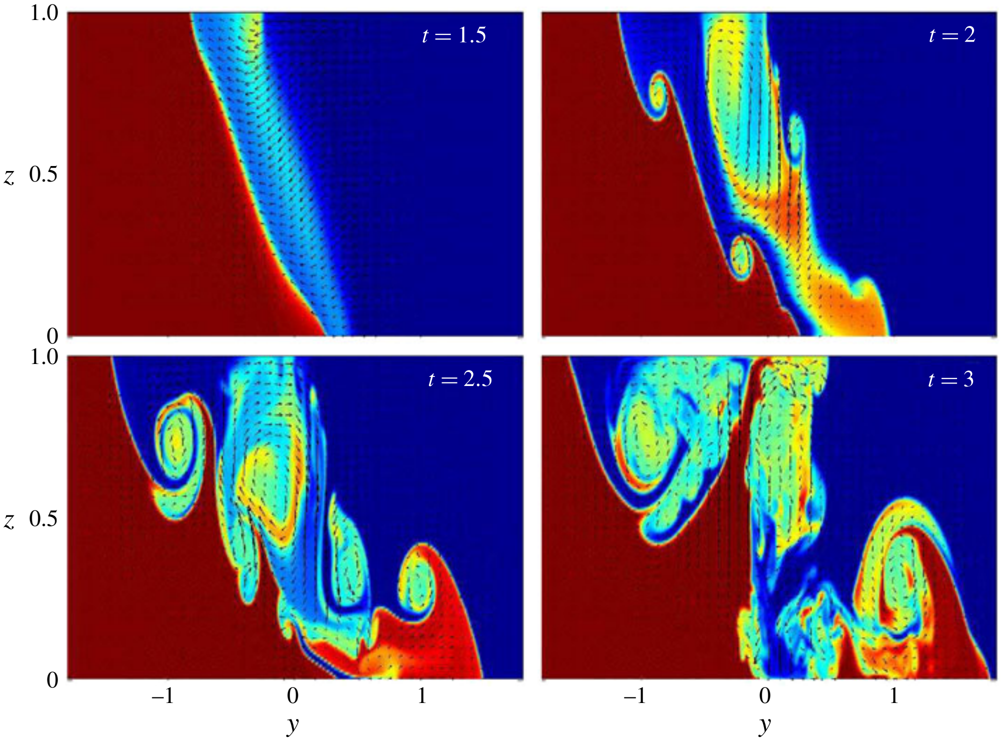

FIGURE 6. Temporal evolution of the buoyancy field in a vertical section at $x = 0.97$ for $\gamma = 0.21$. In-plane velocity vectors shown for reference.

show the in-plane velocity vectors. At $t = 1.5$ there is a patch of dense fluid near the surface near $(y, z) = (-0.2, 1)$ that extends toward the bottom. This feature is formed by the horizontal roll-up of the primary shear vortex (e.g. figure 3*a*). By $t = 2$ the vortex core has developed a distinct overturning circulation through the conversion of vertical vorticity into horizontal vorticity with the tilting of the primary vortex. The patch of dense fluid in the circulation forms a secondary surface front near $y = 0$ where a large vertical current plunges below the surface. There is a returning positive vertical current on the opposite side of the dense feature, within the primary vortex core. Two emerging Kelvin–Helmholtz vortices are also evident. By $t = 2.5$ the vertical overturning circulation in the primary vortex has begun to interact with upper Kelvin–Helmholtz vortex. At $t = 3$ twin, counter-rotating horizontal vortices, one originating from a Kelvin–Helmholtz vortex and the other from the horizontal overturning circulation, produce a large flow between them that pulls dense fluid all of the way to the surface.

4.3. *Evolution of the vorticity*

More insight into the flow can be gained by examining the vorticity dynamics. The production of enstrophy, $\Omega = \omega_i\omega_i/2$, in a Boussinesq, stratified fluid is given (in non-dimensional form using index notation) by

$$\frac{\partial \Omega}{\partial t} + u_j\frac{\partial \Omega}{\partial x_j} = \omega_i\omega_j\frac{\partial u_i}{\partial x_j} + \left(\omega_2\frac{\partial s}{\partial x_1} - \omega_1\frac{\partial s}{\partial x_2}\right) + \nu\frac{\partial^2 \Omega_i}{\partial x_j \partial x_j} - \nu\frac{\partial \omega_i}{\partial x_j}\frac{\partial \omega_i}{\partial x_j}. \tag{4.1}$$

The three terms on the right-hand side are, respectively, production due to stretching and tilting, production due to baroclinic torque, P_B, and viscous diffusion of

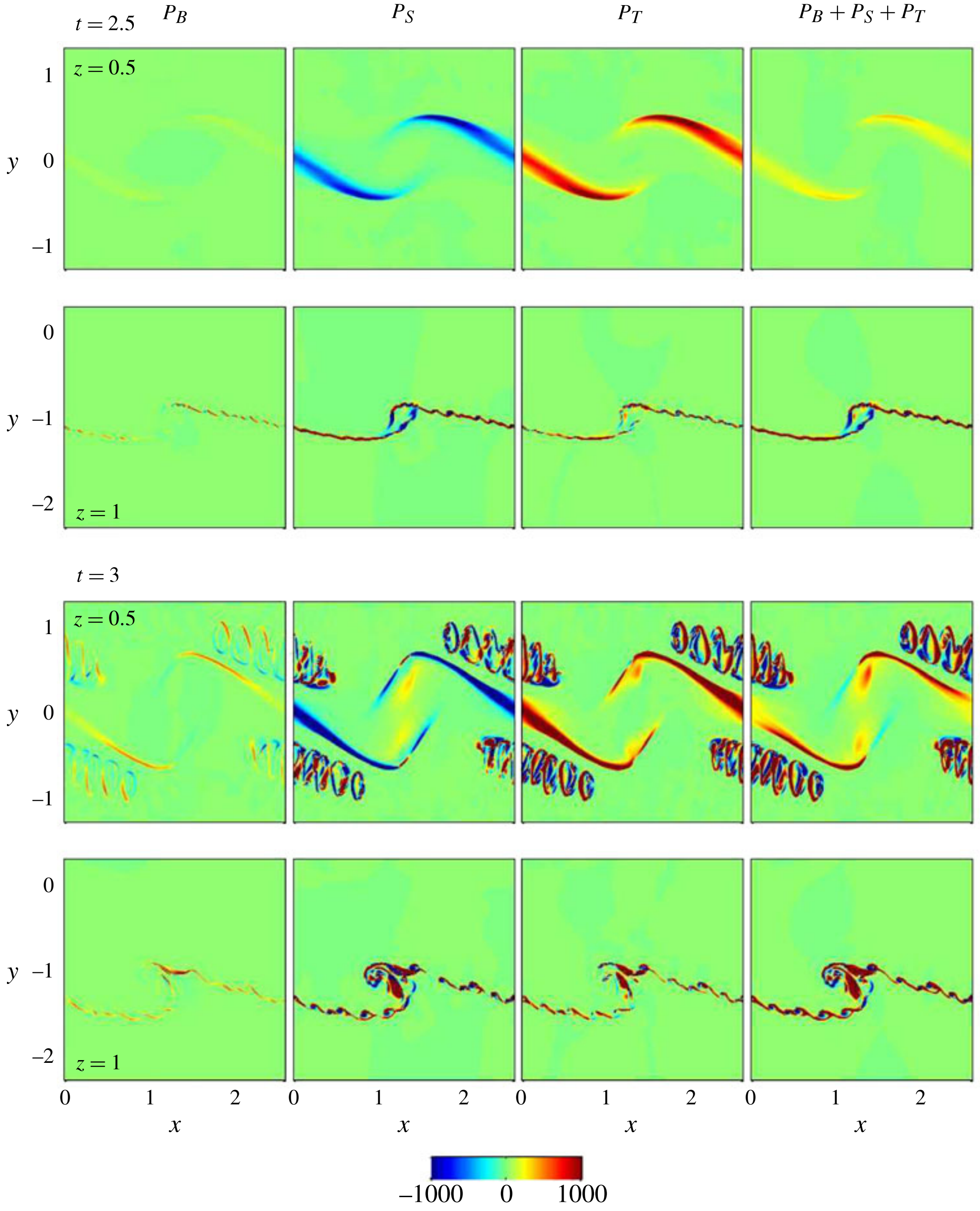

FIGURE 7. Enstrophy production terms for $\gamma = 0.42$: baroclinic, P_B; stretching, P_S; tilting, P_T; and total production at $z = 0.5$ and $z = 1$ for $t = 2.5$ and $t = 3$.

enstrophy and viscous dissipation. The first term on the right-hand side can be decomposed into contributions from stretching and tilting, $\omega_i \omega_j \partial u_i / \partial x_j = P_S + P_T$, where $P_S = \omega_i \omega_i \partial u_i / \partial x_i$.

The contributions of each production term to the growth of the enstrophy for $\gamma = 0.42$ are shown in figure 7. During the initial stage of gravitational adjustment there is vortex compression (negative stretching) in the mid-plane. Compression is evident at the surface ($z = 1$) in the centre region of the shear vortex. However, strong stretching occurs away from the vortex centre. This stretching is a consequence of the frontal convergence and drives the secondary shear-layer roll-up that is just beginning at $t = 2.5$. The rate of enstrophy production is close to 1000 at the surface. A vorticity field with initial magnitude of $O(1)$ can be enhanced by a factor of 10 over a time interval as short as $\mathrm{d}t \sim 0.1$, consistent with the rapid development of the secondary shear vortices. There is considerable vorticity production due to tilting throughout the water column. The total enstrophy production at $z = 0.5$ is positive, as tilting dominates compression. Conversely, the total production at $z = 1$ is dominated by the stretching of the central vortex. This trend was generally observed for all γ in the early stages of flow development. In all cases, the baroclinic production, P_B, is considerably smaller than stretching and tilting (even for large values of γ).

The initial vortex sheet continues to undergo compression in the mid-plane at later times, but there is stretching of the two dislocated primary vortex cores and in the Kelvin–Helmholtz rolls that have emerged by $t = 3$ (figure 7). Tilting production continues along the vortex sheet away from the cores. Overall, tilting exceeds compression, as the total enstrophy grows rapidly throughout the midplane with the exception of a few localized regions. At the surface, stretching dominates tilting, with vortex production maximized near the central core. At later times (not shown) stretching and compression both contribute approximately equally at the mid-plane and surface, as regions of positive and negative vortex production become highly convoluted.

For cases with higher shear (not shown), there can be considerable stretching in the primary vertical vortex. While the relative importance of tilting and stretching vary somewhat for different γ, both processes intensify the vorticity field and lead to turbulence at small scales.

4.4. *Surface expression of the vertical velocity and vorticity*

The observations of Farmer *et al.* (2002) documented very strong near-surface vertical flows (cf. their figure 6) and whirlpools at the surface. The numerical solutions illustrate the mechanisms behind their observations. Vertical vorticity, ω_z, and velocity, w, in y–z cross-sections, are shown for $\gamma = 0.21$ and $\gamma = 0.42$ in figure 8. The sections are located at the x-location of the surface expression of the tilted vortex, $x = 0.97$ and 1.21, respectively. The figures also show the in-plane velocity vectors. In both examples there is a coherent, tilted vortex tube that intersects the surface, ranging between approximately $-0.4 < y < 0$ for $\gamma = 0.21$ and $-1.2 < y < -0.8$ for $\gamma = 0.21$. In each case, the vortex tube is bounded by regions of strong downwelling, near $y = 0$ (-0.8) for $\gamma = 0.21$ (0.42), and strong upwelling, near $y = -0.4$ (-1.2) for $\gamma = 0.21$ (0.42). The vorticity and vertical velocities are particularly strong for $\gamma = 0.21$, with $w \approx -1.5$, which is an order of magnitude larger than the vertical flows at the gravity current surface front ($y \approx -1$). In both cases the downwelling zone reaches from the surface to near mid-depth, in qualitative agreement with the deep bubble plumes observed by Farmer *et al.* (2002). The upwelling and downwelling regions result from the tilting of the primary shear vortex, which converts vertical vorticity to horizontal, with an accompanying overturning (also seen in figure 3(*b*), for example). An alternative interpretation is that upwelling is associated with buoyant fluid moving toward the gravity current surface front with positive w. In the process, it drags upward the dense fluid trapped in the tilted vortex core. Upon reaching the surface the dense fluid is negatively buoyant, and a downwelling flow develops on the opposite side of the vortex core, essentially forming a convection cell. Again figure 3(*b*) is helpful in visualizing this process.

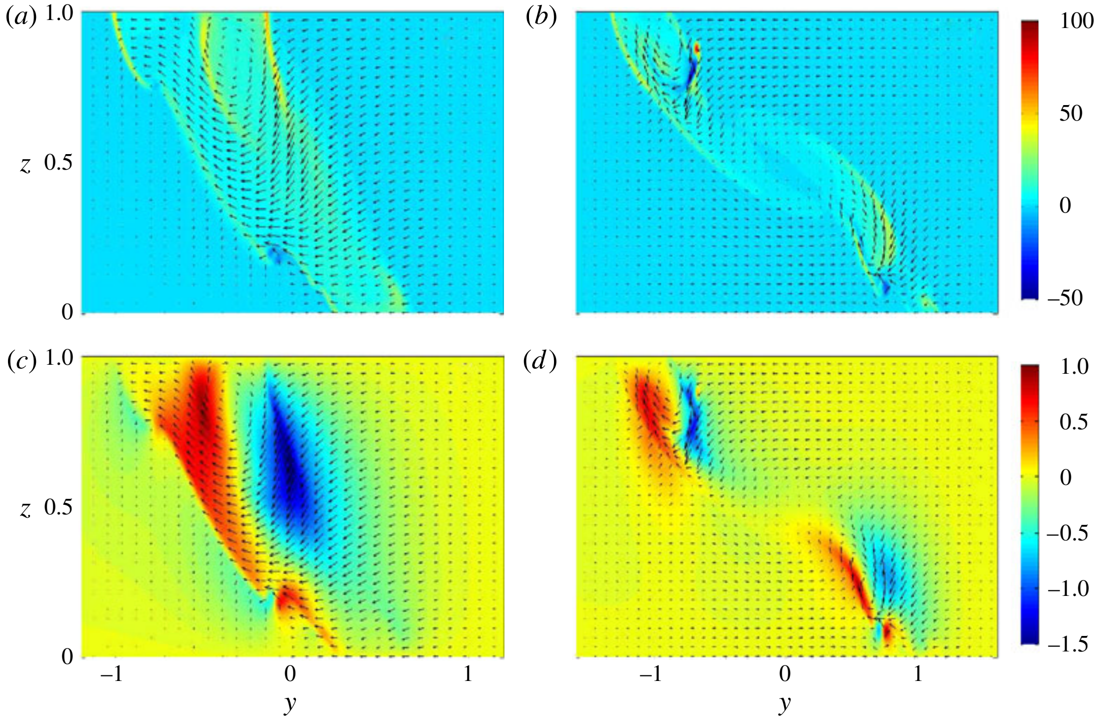

FIGURE 8. Vertical vorticity (*a*,*b*) and vertical velocity (*c*,*d*) in the y–z plane: (*a*,*c*) $\gamma = 0.21$, $x = 0.97$ and $t = 1.75$; (*b*,*d*) $\gamma = 0.42$, $x = 1.21$, and $t = 2.75$. In-plane velocity vectors are also shown.

5. Evolution of the mean velocity and buoyancy profiles

The rapid breakdown of the flow into complex three-dimensional motions leads to rapid mixing of the buoyancy and momentum fields, particularly for small values of γ. Figure 9 shows y–z buoyancy sections at $x = 1.28$ and $t = 4$, and the streamwise-averaged sections at $t = 8$, for $\gamma = 0.1$ to 0.83. The $\gamma = 0.83$ case resembles a pure gravity current with distinct and sharp surface and bottom fronts. However, increasing the shear, $\gamma = 0.42$, 0.21 and 0.10, produces strong turbulent mixing. The x-averaged sections at $t = 8$ show that the buoyancy field becomes mixed over the full depth and the gravity current fronts more diffuse as γ decreases, with an increase in the mean isopycnal slope.

The surface buoyancy front position, y_f, as a function of time is shown in figure 10. Here y_f is the location, for any x, at which the surface buoyancy first decreases below $s = 0.999$. Following an initial transient, the front speeds are close to the ideal gravity current speed, $c_f = 0.5$, for $\gamma \geqslant 0.42$. However, when $\gamma \leqslant 0.21$ the front advance is more rapid. Advection from the strong shear instability and associated mixing make the interface more diffuse, initially increasing the front propagation speed. For $\gamma \geqslant 0.42$ the front eventually adjusts so that for $t > 4$ the speed is close to the ideal gravity current speed. When $\gamma = 0.1$, the front speed for $2 < t < 4$ is $c \approx 1.5$, a factor of three larger than the ideal gravity current. However, the front eventually slows and reaches the domain boundary at $t \approx 6$.

The temporal evolution of the horizontal buoyancy and velocity distributions are shown in figure 11. The x- and z-averaged buoyancy, $\langle s\rangle_{xz}$, and streamwise velocity, $\langle u\rangle_{xz}$, distributions are shown for $\gamma = 0.1$ and 0.83 in figure 11(*a*,*b*), respectively. The angled brackets indicate spatial averaging over the subscript dimensions. The y-profiles

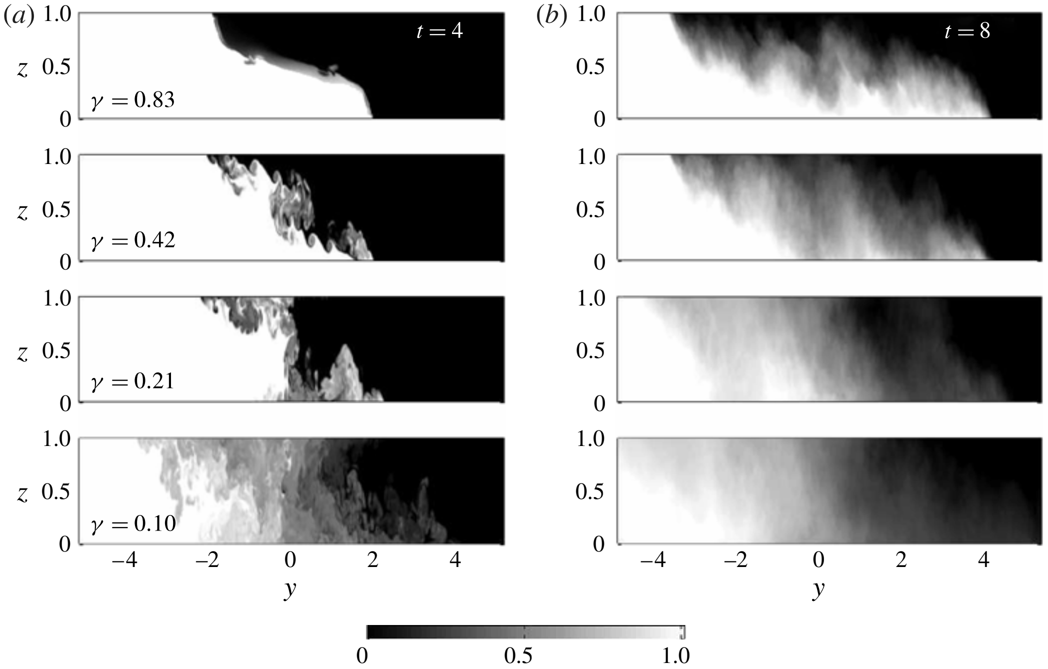

FIGURE 9. Buoyancy sections in the y–z plane. (a) Vertical sections at $x = 1.28$ and $t = 4$ for $\gamma = 0.1$ to 0.83. (b) Streamwise-averaged buoyancy, $\langle s\rangle_x$ ($= \int_0^L s\,\mathrm{d}x$) at $t = 8$ for the same γ values.

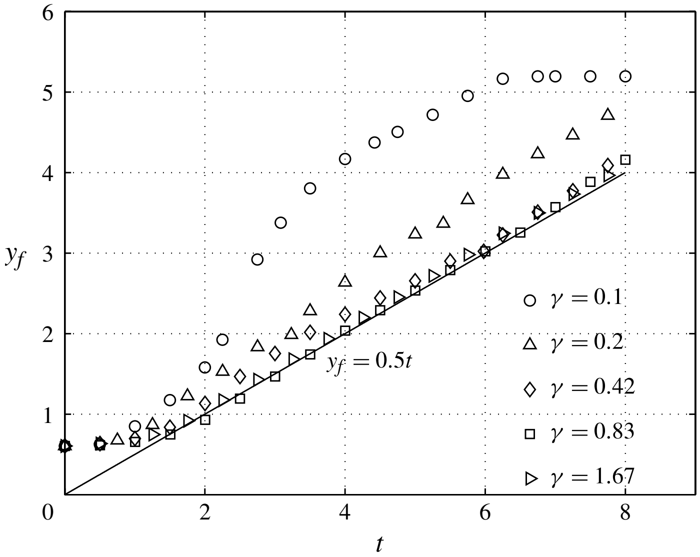

FIGURE 10. Surface front position, y_f, versus time for all γ. The solid line shows the ideal gravity current ($c_f = 1/2$) front position.

of $\langle s\rangle_{xz}$ and $\langle u\rangle_{xz}$ can be compared with a homogenous mixing layer. The latter would evolve as an error function, or similar smooth profile, with characteristic integral width for velocity of $\delta_u(t)$. Here the flow is assessed using an integral width δ_u based on the

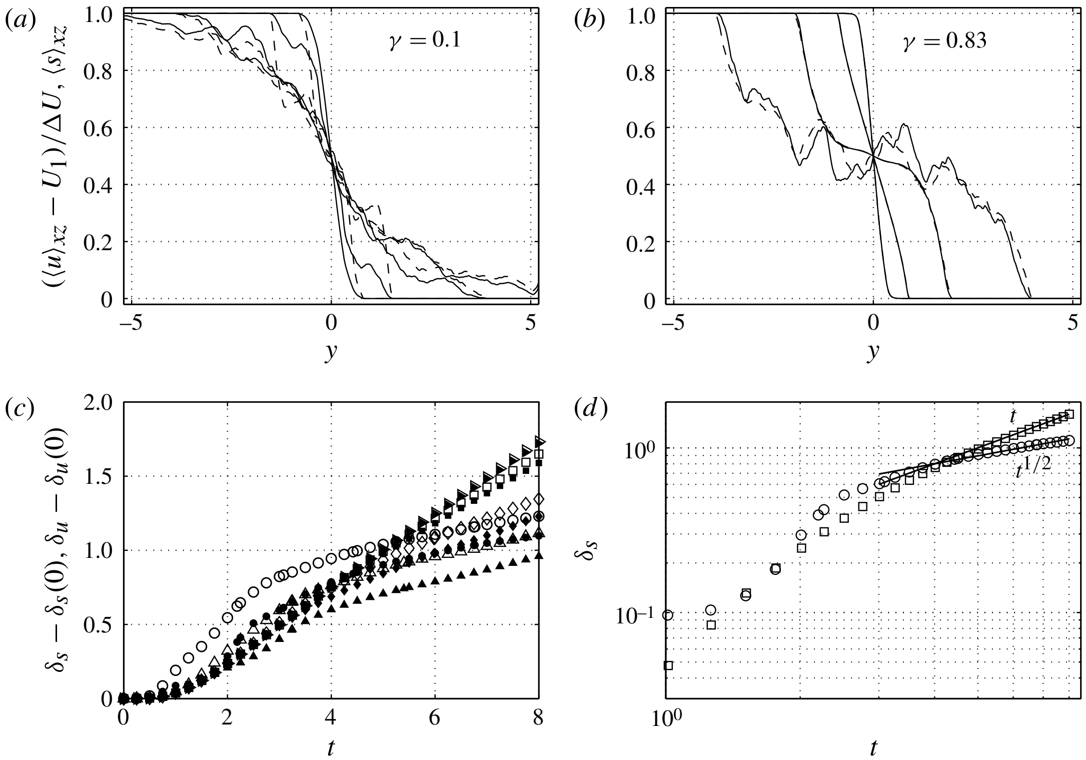

FIGURE 11. Lateral evolution of the mixing layer. Profiles of x and z-averaged streamwise velocity, $\left(\langle u\rangle_{xz} - U_1\right)/\Delta U$ (solid), and buoyancy, $\langle s\rangle_{xz}$ (dashed), for (*a*) $\gamma = 0.1$ and (*b*) $\gamma = 0.83$ at $t = 1$, 2, 4, 8 (bottom and top fronts advance monotonically). (*c*) Evolution of the mixing layer thickness for velocity, δ_u (closed symbols), and buoyancy, δ_s (open symbols), for all γ. Matching open and closed symbols correspond to the same values of γ. The symbols are the same as in figure 10. (*d*) Log–log plots of δ_s for $\gamma = 0.1$ (○) and $\gamma = 0.83$ (□). Solid lines show the $\delta_s \sim t$ behaviour for $\gamma = 0.83$ and $\gamma \sim t^{1/2}$ behaviour for $\gamma = 0.1$.

momentum thickness for $\langle u\rangle_{xz}$,

$$\delta_u = \int_{-L_y}^{L_y} \frac{1}{4}\left(\langle u\rangle_{xz} + 1\right)\left(1 - \langle u\rangle_{xz}\right)\, \mathrm{d}y, \tag{5.1}$$

and an analogous integral width, δ_s, for buoyancy $\langle s\rangle_{xz}$,

$$\delta_s = \int_{-L_y}^{L_y} \langle s\rangle_{xz}(1 - \langle s\rangle_{xz})\, \mathrm{d}y. \tag{5.2}$$

At $\gamma = 0.1$, for which there is strong vertical mixing, the lateral profiles of buoyancy and velocity (figure 11*a*) do resemble an error function, with some fluctuations. The buoyancy field spreads slightly faster than the velocity, which can be seen from the plots of $\langle u\rangle_{xz}$ and $\langle s\rangle_{xz}$ in figure 11(*a*) and from the evolution of δ_u and δ_s in figure 11(*c*). The $\gamma = 0.83$ case is different. The signature of a gravity current is evident in the profiles of $\langle u\rangle_{xz}$ and $\langle s\rangle_{xz}$ (figure 11*b*), a consequence of the weaker mixing and greater vertical and horizontal stratification.

The distinction between strong and weak shear is evident in the evolution of $\delta_u(t)$ and $\delta_s(t)$ shown in figure 11(*c*). For large γ (weak shear), δ_u and δ_s both increase linearly with time (cf. figure 10), whereas for $\gamma = 0.1$ and 0.21 the growth of δ_u and δ_s

decreases with time. Figure 11(*d*) compares the growth of δ_s for $\gamma = 0.1$ and 0.83. For both, there is an initial period of rapid increase for $t \lesssim 3$. The behaviour then crosses over to $\delta_s \sim t$ for $\gamma = 0.83$, indicative of steady gravity current propagation. However, for $\gamma = 0.21$, the scaling transitions to a diffusive-like regime $\delta_s \sim t^{1/2}$. This difference in behaviour is related to the degree of vertical mixing, discussed in greater detail in § 7.

6. Energetics

Further insight into this complex flow can be gained from the evolution of the energy budgets. When averaged over the computational domain, the (non-dimensional) kinetic energy budget is governed by

$$\frac{\mathrm{d}E_k}{\mathrm{d}t} = -\langle sw \rangle - \varepsilon_v \tag{6.1}$$

where the volume-averaged kinetic energy is

$$E_k = \left\langle \frac{1}{2}\boldsymbol{u}\cdot\boldsymbol{u} \right\rangle = \frac{1}{V}\int_V \frac{1}{2}\left(u^2+v^2+w^2\right)\,\mathrm{d}V, \tag{6.2}$$

$\langle sw \rangle$ is the volume-averaged buoyancy flux. The dissipation of kinetic energy is given by

$$\varepsilon_v = \frac{1}{Re}\left\langle \frac{\partial u_i}{\partial x_j}\frac{\partial u_i}{\partial x_j} \right\rangle. \tag{6.3}$$

However, in the ILES simulations the explicit viscosity is set to zero ($Re \rightarrow \infty$), so ε_v is calculated as the residual from (6.1).

The evolution of volume-averaged potential energy,

$$E_p = \frac{1}{V}\int_V sz\,\mathrm{d}V = \langle sz \rangle, \tag{6.4}$$

is governed by

$$\frac{\mathrm{d}E_p}{\mathrm{d}t} = \langle sw \rangle + D_p. \tag{6.5}$$

Here D_p denotes the conversion of internal to potential energy, independent of macroscopic fluid motion (Peltier & Caulfield 2003). Winters *et al.* (1995) showed that for a fixed domain this term is given by

$$D_p = \kappa \oint_S z\nabla s\cdot\boldsymbol{n}\,\mathrm{d}S - \kappa\int_A (s_{top} - s_{bottom})\,\mathrm{d}A. \tag{6.6}$$

Here κ is the (non-dimensional) molecular scalar diffusivity, S is the bounding surface of the domain, $\boldsymbol{n}$ is the surface normal and A is the horizontal area of the domain. As with viscosity, κ is set to zero in the ILES simulations, so D_p is found as the residual of (6.5).

Because the buoyancy flux contains both reversible motions (stirring) and irreversible conversion (mixing) it is useful to separate the potential energy into an available component, E_a, and a background component, E_b, so that $E_p = E_a + E_b$. Winters *et al.* (1995) introduced the concept of a background potential energy, which is the minimum potential energy attainable through an adiabatic redistribution of the buoyancy field. The redistributed buoyancy field, $s_*(z_*)$, is obtained from vertically

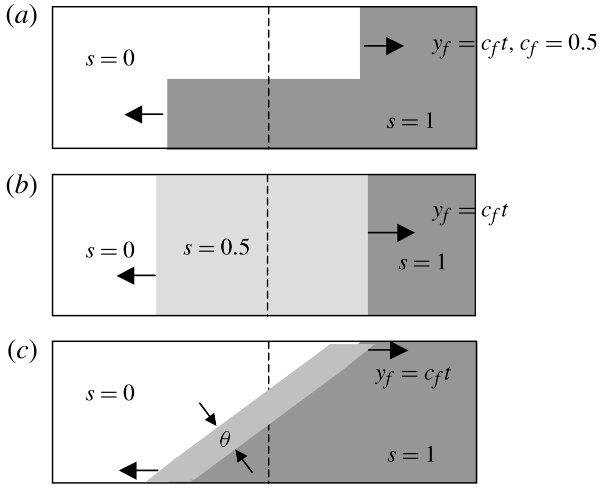

FIGURE 12. Schematic illustration of (*a*) ideal gravity current, (*b*) ideal mixing layer and (*c*) transitional behaviour.

stacking all buoyancy elements and stretching each one to fill the entire horizontal domain. The resorting is a mapping, $z_*(x, y, z)$, which gives the vertical position in the re-sorted state of the fluid element at position (x, y, z). The background potential energy is thus given by

$$E_b = \frac{1}{V}\int_V s_*(z_*)z_*\,\mathrm{d}V = \int_0^1 z_* s_*(z_*)\,\mathrm{d}z_*, \tag{6.7}$$

where the second equality derives from the fact that $\mathrm{d}z_* = \mathrm{d}z/A$ (where A is the horizontal area).

The temporal evolution of E_a, i.e. the stirring rate, is given by

$$\frac{\mathrm{d}E_a}{\mathrm{d}t} = \langle sw\rangle - M, \tag{6.8}$$

where M is the rate of irreversible mixing due to fluid motion. The background potential energy gain, i.e. the total irreversible mixing rate, is given by

$$\frac{\mathrm{d}E_b}{\mathrm{d}t} = M + D_p. \tag{6.9}$$

For the tilting horizontal shear flow, these energy budgets can be viewed in light of two end-member cases: an ideal, non-mixing gravity current and an ideal mixing layer (figure 12*a*,*b*). First consider the ideal gravity current without horizontal shear, for which there is a perfect conversion of initial potential energy to kinetic energy as the gravity current propagates. Without mixing, $E_p = E_a$ and $\mathrm{d}E_k/\mathrm{d}t = -\mathrm{d}E_p/\mathrm{d}t = -\langle sw\rangle$. Available potential energy is released at a rate that depends on the front speed, c_f.

In a time $\mathrm{d}t$, a volume, $\mathrm{d}V = HL_x c_f\,\mathrm{d}t/2$, of initially motionless dense ($s = 1$) fluid in the upper half of the domain is replaced by an equivalent volume of light ($s = 0$) fluid moving with the gravity current front speed, c_f. At the same time the same volume of light fluid is replace by dense fluid moving along the bottom half of the domain. The associated change in potential energy is $-L_x Hc_f\,\mathrm{d}t/4$. Using the ideal gravity current speed $c_f = 1/2$ and averaging over the domain volume $2L_yL_xH$, gives

$$\frac{\mathrm{d}E_p}{\mathrm{d}t} = \frac{\mathrm{d}E_a}{\mathrm{d}t} = \langle sw \rangle = -\frac{1}{16L_y}. \tag{6.10}$$

Conservation of total energy gives

$$\frac{\mathrm{d}E_k}{\mathrm{d}t} = -\frac{\mathrm{d}E_p}{\mathrm{d}t} = -\langle sw \rangle = \frac{1}{16L_y}. \tag{6.11}$$

The other limit is an ideal, completely mixed region between the two propagating fronts (figure 12*b*). A volume $V = HL_xc_f\,\mathrm{d}t$ of dense ($s = 1$) fluid has an initial potential energy $sz_oV = c_f\,\mathrm{d}tL_xH/2$, where $z_o = 0.5$ is the centre of mass. After it has completely mixed with an equivalent volume of light ($s = 0$) fluid, the buoyancy $s = 0.5$ and the potential energy is $sz_o2V = c_f\,\mathrm{d}tL_xH/2$, since $z_o = 0.5$. There is no change in potential energy, no net buoyancy flux ($\langle sw \rangle = 0$) and no net exchange between the kinetic and potential energy reservoirs. There is, however, a complete conversion of available to background potential energy. Initially, in the volume $2HL_xc_f\,\mathrm{d}t$, the available potential energy is $c_f\,\mathrm{d}tL_xH/4$. Therefore, after dividing by the total domain volume and again taking $c_f = 1/2$,

$$\frac{\mathrm{d}E_b}{\mathrm{d}t} = -\frac{\mathrm{d}E_a}{\mathrm{d}t} = \frac{1}{16L_y}. \tag{6.12}$$

A summary of the volume-averaged energetics for all of the numerical runs are shown in figure 13. The total kinetic and potential energies, the buoyancy flux, the viscous (ILES) dissipation and the evolution of available and background potential energies shed light on the dominant energy transfers, which vary considerably across the parameter space. The $\gamma = 1.67$ case is consistent with an ideal gravity current. Energy is transferred from kinetic to potential energy by the buoyancy flux, $\mathrm{d}E_k/\mathrm{d}t \approx -\mathrm{d}E_p/\mathrm{d}t \approx -\langle sw \rangle$, very close to $\langle sw \rangle = -0.0120$ from (6.11) with $L_y = 5.2$. There is little increase in background potential energy since there is little turbulent mixing. With increasing shear (smaller γ) there is more irreversible mixing and dissipation of kinetic energy. For $\gamma = 0.83$, 0.42 and 0.21, there is an initial, primarily inviscid adjustment period during which the behaviour is close to an ideal gravity current, as potential energy is transferred to kinetic energy and the buoyancy flux is close to the ideal limit. The duration of this period decreases with increasing shear. The subsequent onset of the horizontal shear and Kelvin–Helmholtz instabilities and resulting turbulent breakdown causes a rapid decay of the kinetic energy, a decrease of the buoyancy flux and a reduction in the rate of potential energy loss.

The highest shear case, $\gamma = 0.1$, shows an even greater effect of the shear instability. The potential energy decreases with a corresponding increase in E_k during the initial slumping. After $t \approx 3$, the potential energy becomes approximately constant, resembling the mixing layer model in figure 12(*b*). The buoyancy flux reaches large negative values, $\langle sw \rangle \approx -0.02$ ($t \approx 1$), that exceed all other cases. The shear instability dominates the buoyancy adjustment even at early times. Shortly thereafter, $\langle sw \rangle$ rapidly becomes positive ($t \approx 2$–3) as turbulent mixing causes an upward flux of dense fluid. The buoyancy flux also becomes positive for $t \approx 3$–4 at $\gamma = 0.21$. For both of these cases the buoyancy flux becomes negative again as the implicit numerical dissipation of kinetic energy dominates the energetics, and mixing of the buoyancy field decreases (see § 6). Only with large shear, $\gamma \leqslant 0.21$, does the buoyancy flux

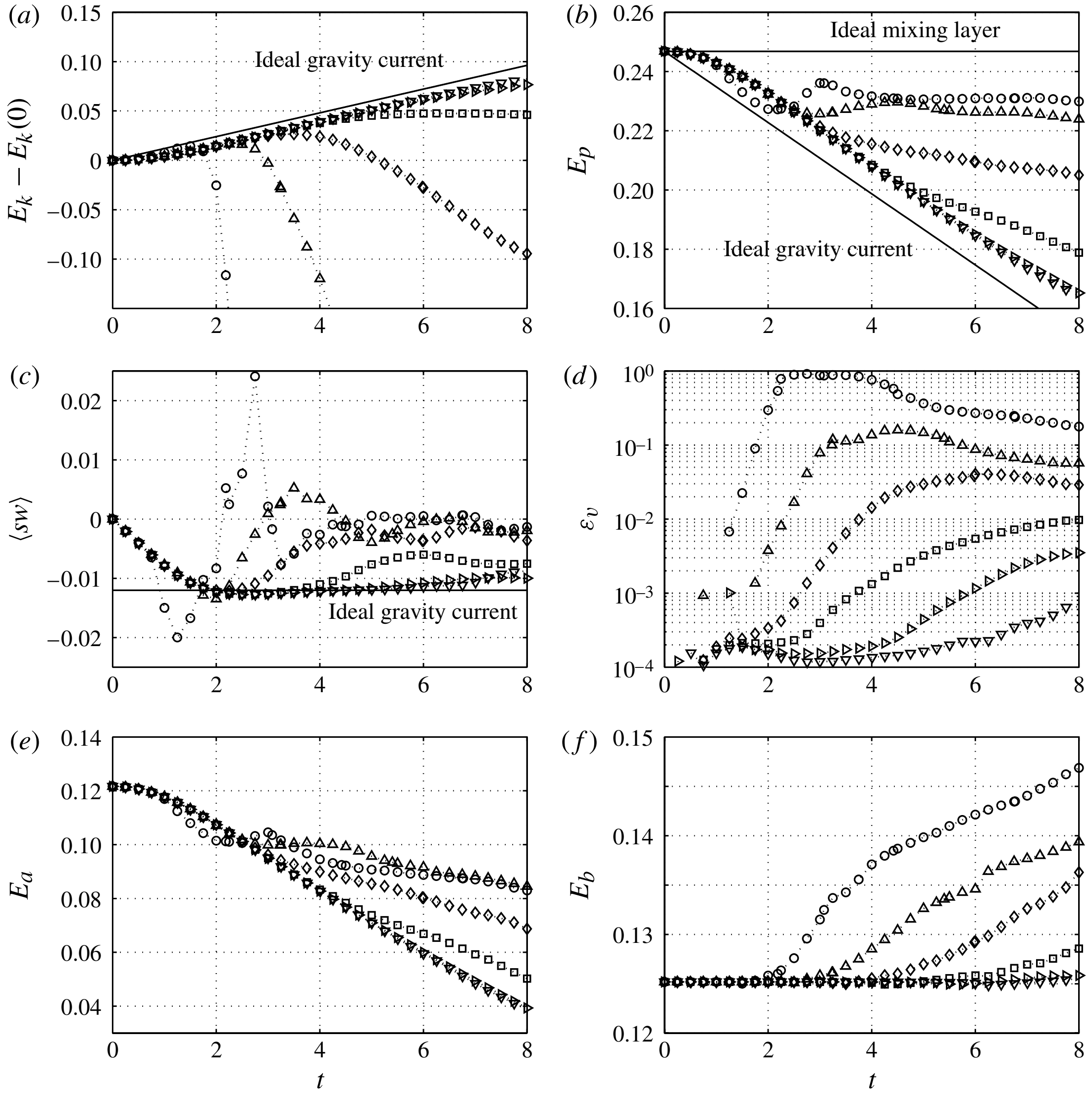

FIGURE 13. Energy budgets for: (○) $\gamma = 0.1$; (△) $\gamma = 0.21$; (◇) $\gamma = 0.42$; (□) $\gamma = 0.83$; (▷) $\gamma = 1.67$; and (▽) $\gamma \to \infty$. (*a*) Kinetic energy. (*b*) Potential energy. (*c*) Buoyancy flux. (*d*) Viscous dissipation of kinetic energy. (*e*) Available potential energy. (*f*) Background potential energy. The ideal gravity current and mixing layer models are indicated.

become significantly positive. For the other cases, the negative buoyancy flux from the gravitational adjustment overcomes any positive contribution from turbulent mixing.

The two highest shear cases exhibit an initial rapid increase in the implicit viscous dissipation, corresponding to the initial period when potential energy is released and kinetic energy grows. The kinetic energy and viscous dissipation peak at $t \approx 2$ (3) for $\gamma = 0.1$ (0.21). It is around the time of this peak that the rate of growth of E_b is the largest and the rate of decrease of E_a is greatest. Subsequently, a rough balance develops between the decrease of E_a and the slower growth of E_b. At the same time, ε_v and E_k decrease, indicative of decaying turbulence. This period, when the drop in E_a and rise in E_b are in approximate balance, corresponds to the period of diffusive mixing discussed in § 7.

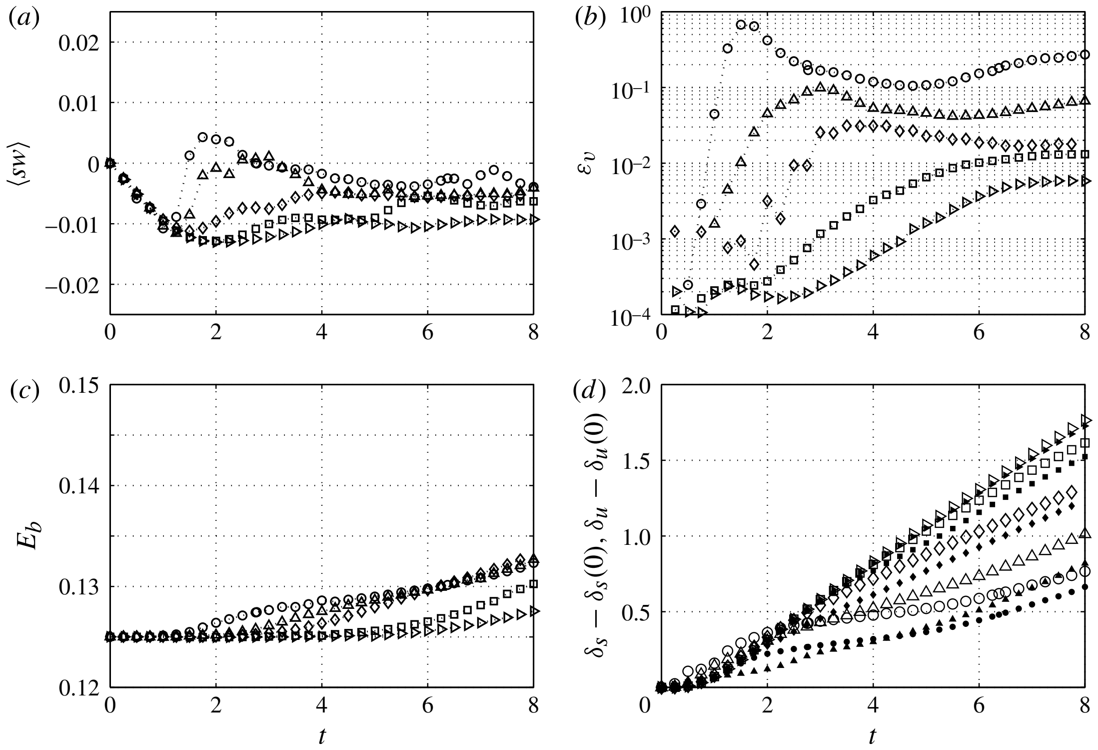

FIGURE 14. Energy and mixing characteristics of $l_u = 1/12$ simulations: (○) $\Delta U = 8$, $\gamma = 0.05$; (△) $\Delta U = 4$, $\gamma = 0.1$; (◇) $\Delta U = 2$, $\gamma = 0.21$; (□) $\Delta U = 1$, $\gamma = 0.42$; (▷) $\Delta U = 0.5$, $\gamma = 0.83$. (*a*) Buoyancy flux. (*b*) Viscous dissipation. (*c*) Background potential energy. (*d*) Mixing layer thickness for velocity, δ_u (closed symbols), and buoyancy, δ_s (open symbols).

6.1. *Effects of initial interface thickness*

A small number of simulations were run with a thinner initial interface, $l_u = 1/12$, to assess the importance of this parameter, independent of γ. Results for selected terms in the energy budget and the mixing layer thicknesses, δ_u and δ_s, are shown in figure 14. The results are qualitatively similar to the $l_u = 1/6$ cases. Comparison of the viscous dissipation, for example, suggests that the thinner interface cases are developing faster, as would be expected by the faster shear time scale, $l_u/\Delta U$. The increase in background potential energy is in general less for each γ than for the $l_u = 1/6$ cases, an issue we address in the next section on mixing.

7. Mixing

Because the buoyancy flux remains negative, except during brief periods for $\gamma = 0.1$ and 0.21, $\langle sw \rangle$ is not a good mixing diagnostic. A better measure is the rate of increase of background potential energy, which measures irreversible mixing and whose growth rate is positive definite.

As the flow develops, mixing results in a re-sorted buoyancy profile, $s_*(z_*, t)$, with an increasingly thick interface separating bottom ($s_* = 1$) and top ($s_* = 0$) fluid, which grows monotonically (figure 15*a*). The function $1 - s_*(z_*)$ can be interpreted as a cumulative distribution function for the arrangement of fluid parcels (sorted by buoyancy from $s = [0, 1]$ with z_* playing the role of the random variable).

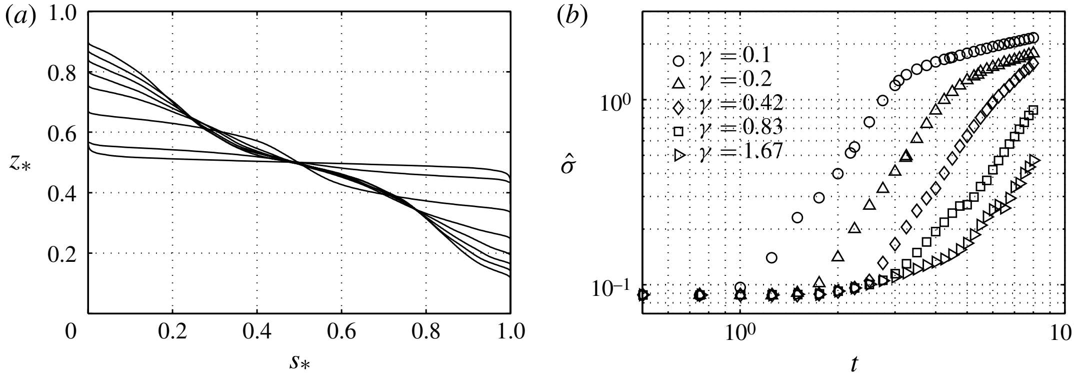

FIGURE 15. Evolution of the background buoyancy profile and the growth of the mixed region. (*a*) Sorted background buoyancy field $s_*(z_*)$ for $\gamma = 0.1$ at $t = 1{:}1{:}8$ (with monotonically increasing z_*-intercept). (*b*) Mixed layer thickness $\hat{\sigma}$ for the indicated γ.

The corresponding probability density function (p.d.f.) $f = -\partial s_*/\partial z_*$ describes the distribution of mixed fluid around the centre of mass, $z_* = 0.5$. The standard deviation of this p.d.f. can be used as a measure of interface thickness. For a general distribution $s_*(z_*)$, for which $s_*(0) \to 0$, $s_*(1) \to 1$ and $\partial s_*/\partial z_* \to 0$ for $z_* = 0$ and 1, the variance of the corresponding p.d.f. is

$$\sigma^2 = \int_0^1 -\frac{\partial s_*}{\partial z_*} z_*^2 \, \mathrm{d}z_*' - \left[\int_0^1 -\frac{\partial s_*}{\partial z_*} z_* \, \mathrm{d}z_*'\right]^2 = 2\int_0^1 s_* z_* \, \mathrm{d}z_*' - \left(\frac{1}{2}\right)^2 = 2E_b - \frac{1}{4}. \quad (7.1)$$

Hence, the background potential energy is an integral measure of the thickness of mixed fluid. For example, if $s_*(z_*, t)$ follows an error function profile,

$$s_*(z_*, t) = \frac{1}{2}\left[1 - \mathrm{erf}\left(\frac{z_* - 0.5}{\sqrt{2}\sigma(t)}\right)\right], \quad (7.2)$$

then the p.d.f. is a Gaussian function with variance σ^2. Of course, $s_*(z_*, t)$ from the numerical runs do not behave as error functions. Figure 15(*a*) shows that $s_*(z_*, t)$ for $\gamma = 0.1$ is closer to a piecewise linear function. Regardless of the profile details, $\sigma(t)$ from (7.1) gives a well-defined integral thickness and a measure of the mixing.

An effective 'vertical' diffusivity, K_{z_*}, can be defined from the mean-square growth of variance according to the standard definition,

$$K_{z_*} = \frac{1}{2}\frac{\mathrm{d}\sigma^2}{\mathrm{d}t} = \frac{\mathrm{d}E_b}{\mathrm{d}t}. \quad (7.3)$$

A drawback of σ from (7.1) as a metric for mixing is that it is domain-averaged and therefore depends on L_y. To illustrate, the total volume of mixed fluid at time t is $2L_yL_x\sigma(t)$. The rate at which this volume grows (measured by $\mathrm{d}\sigma/\mathrm{d}t$ or by K) increases with the tilting and stretching of the interface, i.e. the length of the $s = 0.5$ contour. This interface grows from its initial area of L_xH to approximately $2L_xy_f(t)$ (see figure 12*c*). If the physical thickness of the mixed region is $\theta(t)$, then the total mixed fluid volume should grow as $2y_fL_x\theta(t)$ and, hence, $\sigma(t) \sim \theta(t)y_f(t)/L_y$, i.e. σ depends on domain size and grows with y_f as the front advances.

Ideally, a measure for mixing should be independent of the undisturbed fluid region beyond the surface and bottom fronts. To remove the dependence on L_y, we normalize the mixing rate by the vertical cross-sectional area, $L_xH = L_x$ $(H = 1)$

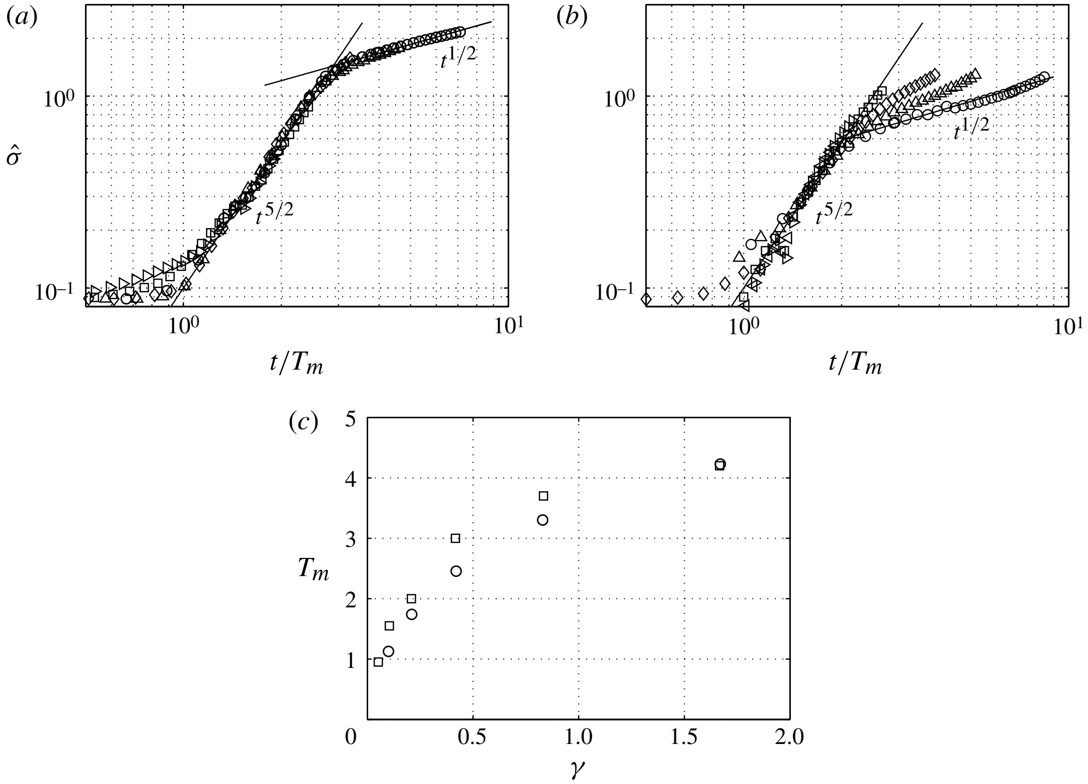

FIGURE 16. Mixed layer thickness versus rescaled time t/T_m: (*a*) $l_u = 1/6$ runs, symbols as in figure 13; (*b*) $l_u = 1/12$ runs, symbols as in figure 14. The regression $\hat{\sigma} = 0.1\,(t/T_m)^{5/2}$ is shown in (*a*) and (*b*). The $t^{1/2}$ regressions are shown for the $\Delta U = 8$ cases, $\hat{\sigma} = \alpha t^{1/2}$ with $\alpha = 0.77$ for (*a*) and $\alpha = 0.43$ for (*b*). (*c*) Mixing time scale T_m versus γ for: (○) $l_u = 1/6$ runs and (□) $l_u = 1/12$ runs.

rather than the horizontal area $2L_yL_x$, and define a new mixing layer thickness $\hat{\sigma} = 2L_yL_x\sigma/L_x = 2L_y\sigma \sim \theta y_f$. Here $\hat{\sigma}$ represents the width in the y-direction over which the fluid is completely mixed in the x–z plane. If $\hat{\sigma} = 2L_y$ then the fluid is fully mixed. We can interpret the corresponding mixing rate, $\hat{K} = (1/2)\mathrm{d}\hat{\sigma}^2/\mathrm{d}t = 4L_y^2K_{z*}$ as a horizontal diffusivity. This approach is consistent with the conceptual picture in figure 12(*c*), as it assesses the rate at which mixed fluid is formed between the two evolving fronts.

Figure 15 shows the evolution of the mixed region for $l_u = 1/6$. The evolving $s_*(z_*)$ profiles are shown for $\gamma = 0.1$ in figure 15(*a*). The growth of $\hat{\sigma}$ is shown in figure 15(*b*) for a range of γ. The total mixing, i.e. the total increase in $\hat{\sigma}$, is largest for small γ. The mixing is also initiated earlier for small γ. There appears to be a time scale, which we call T_m, that determines the time of onset of significant mixing. Once mixing sets in, the slopes of $\hat{\sigma}$ versus t are similar in log–log space, and follow approximately a $t^{5/2}$ initial scaling. This exponent, and the time scale, T_m, are found for each case by regression. Specifically, T_m is defined as the time at which $\hat{\sigma}$ first exceeds 0.1, and can be viewed as an x-intercept of the initial $\hat{\sigma} \sim t^{5/2}$ curve. The reason for this specific scaling is still unclear, but some discussion follows below.

We find that the growth of the mixed region in the initial period collapse very well when time is renormalized as t/T_m and follow closely the $\hat{\sigma} = (t/T_m)^{5/2}$ curve (figure 16*a,b*) for both the $l_u = 1/6$ and $l_u = 1/12$ simulations. Recall from the discussion above that $\hat{\sigma} \sim y_f \theta$. A simple assumption for mixing would be that the interface thickness, i.e. θ, grows diffusively, $\theta \sim t^{1/2}$ as the interface spreads horizontally. With the front propagation $y_f \sim t$, this would give a total mixed layer thickness of $\hat{\sigma} \sim t^{3/2}$. However, the $\hat{\sigma} \sim t^{5/2}$ for early times implies that the interface thickens much faster than diffusively. This is consistent with the rapid development of three-dimensional turbulent structures that quickly span the full depth. Interestingly, the $\hat{\sigma} \sim t^{5/2}$ behaviour is seen for all γ. However, it sets in later (greater T_m) for larger γ, suggesting that the shear instability must reach a critical stage of development before the scaling is observed, since the time scale for shear instability increases with γ.

The time scale, T_m is shown in figure 16(*c*) for all cases. There is a strong trend of increasing T_m with increasing γ that is similar for the $l_u = 1/6$ and $l_u = 1/12$ cases. This trend, together with the collapse with the $t^{5/2}$ scaling, suggests the early development of mixing is strongly correlated to γ, and the competition between shear layer development and gravity current propagation time scales that this time scale represents.

In figure 16(*a*,*b*) there is a change in scaling for $\hat{\sigma}$ at later times. For the $l_u = 1/6$ simulations, the curves collapse and crossover to $\hat{\sigma} \sim t^{1/2}$ scaling. However, note that only the $\gamma = 0.1$ and 0.21 cases extend into this regime (higher γ cases end while still in the $t^{5/2}$ regime). This $t^{1/2}$ scaling could be interpreted as a transition to a horizontally diffusive mixing regime. For these $\gamma = 0.1$ and 0.21 cases, the fluid is rapidly mixed in the vertical (see figure 9), consistent with a picture of horizontal diffusive spreading. The diffusive scaling is also consistent with the horizontal mixing layer growth, $\delta_s \sim t^{1/2}$ growth (figure 11*c*). On the other hand, the $l_u = 1/12$ simulations do not collapse at longer times, even though the $\Delta U = 8$ ($\gamma = 0.05$) and $\Delta U = 4$ ($\gamma = 0.1$) cases do begin to show a $t^{1/2}$, diffusive scaling. Based on the comparison between the two sets of simulations, there appears to be an additional dependence on l_u during later times that is not accounted for in the parameter γ. It is this later dependence that would determine the eventual mixing rate. For example, the horizontal diffusivity, $\hat{K}$, can be calculated from the diffusive scaling, $\hat{\sigma} = (2\hat{K}t)^{1/2}$, and for the $\gamma = 0.1$, $l_u = 1/6$ case $\hat{K} \approx 0.30$ while for both the $\Delta U = 4, \gamma = 0.1$ and the $\Delta U = 8, \gamma = 0.05$, $l_u = 1/12$ cases, $\hat{K} \approx 0.10$. This suggests a clear dependence on l_u, which is reasonable to expect since l_u establishes the size of the primary shear vortices, which are increasingly important for small γ.

In contrast to the classic situation with both vertical shear and stratification, horizontal shear layers with horizontal stratification develop rapidly as the interfacial area grows to fill the domain. If the rate of shear is large enough (small γ) the mixing appears to cross over to a regime characterized by horizontal diffusion. It is unclear whether flows with large γ will produce this cross-over. Presumably as the flow approaches the gravity current limit, the front propagation is faster than the vertical mixing rate. Simulations with longer times and larger domain sizes would be necessary in order to assess whether cases with intermediate values of γ ever exhibit the diffusive behaviour and whether a critical value of γ separates the two behaviours. Linden & Simpson (1986), in their study of gravity currents subjected to strong mixing, found a similar cross-over from a slumping-dominated to a vertically mixed horizontal diffusive regime, over a time scale (or length of frontal propagation) that decreased with stronger mixing. Together with that study, the present results, and particularly the common initial scaling, suggest that the dynamics of the initial

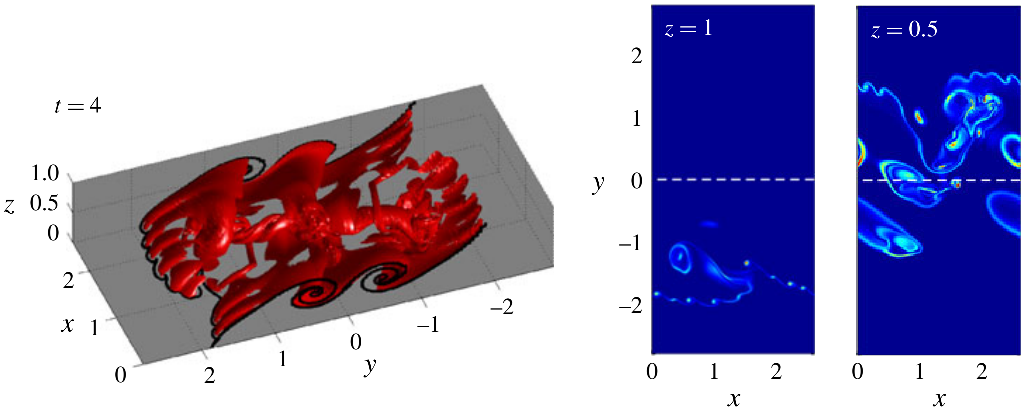

FIGURE 17. Vorticity structure for $\gamma = 0.42$ from DNS. All scales are as in figure 2.

mixing phase and transition to turbulence are complex in gravity currents with external sources of mixing.

8. Comparison between ILES and DNS

It is useful to provide some comparison between the ILES results and a DNS approach. As discussed in § 3, we conducted DNS for the $\gamma = 0.42$ case with fixed viscosity, $\nu = 0.00025$, and Prandtl number, $Pr = \nu/\kappa = 1$, to give a Reynolds number of 4000. The resolution of the DNS run was 384 × 1536 × 192 ($L_x \times L_y \times L_z$) and with slope limiting turned off in the Godunov advection scheme. The results of the comparison with the ILES for the $\gamma = 0.42$ case are shown in figures 17 and 18. This case would be expected to pose the greatest challenge in terms of resolution because the gravitational and shear effects are comparable and the full range of instabilities are present. By comparing the vorticity structure in figure 17 with the ILES results in figure 2, it is clear that the main features of the flow, e.g. the primary shear vortex, the secondary instabilities along the front, and the Kelvin–Helmholtz billows associated with the gravity current, are captured by each approach. The total rate of irreversible mixing, $M + D_p$, and viscous dissipation, ε_v, are compared in figure 18(*a,b*). The ILES and DNS agree very closely both in the overall evolution and the peak values. These two metrics in particular are the most sensitive to differences between the ILES/DNS approach because they depend on gradients at the grid resolution scale. In figure 18(*c*), the dissipation for the DNS is calculated in two ways: the first as the residual of the resolved kinetic energy budget, the second as the explicit viscous dissipation based on the resolved velocity gradient tensor, $\varepsilon = \nu\mathscr{D}$, where $\mathscr{D} = \int_V \boldsymbol{u} \cdot \nabla^2 \boldsymbol{u}\, \mathrm{d}V$. The two estimates agree very closely (at worst the resolved dissipation is ≈85 % of the residual), support that the DNS is well resolved and not simply a viscous ILES (Aspden *et al.* 2008).

The Kolmogorov microscale is shown in figure 18(*c*) for both DNS and ILES. For the DNS η is calculated both explicitly, as $\eta = \nu^{3/4}/\varepsilon^{1/4}$, and based on the resolved velocity gradient tensor, i.e. $\eta = \varepsilon^{1/2}/\mathscr{D}^{3/4}$ (as discussed in § 3), while for ILES η is calculated with the latter. For later times (after $t \approx 4$) the effective value of η is very similar for the ILES and DNS, suggesting the Reynolds number range for the DNS is appropriate for comparison with the ILES (as also illustrated by the similarity in the dissipation shown in figure 18*b*). The Kolmogorov scales can be compared with the horizontal grid resolutions, 0.0068 for DNS and 0.0102 for ILES. For the DNS, the

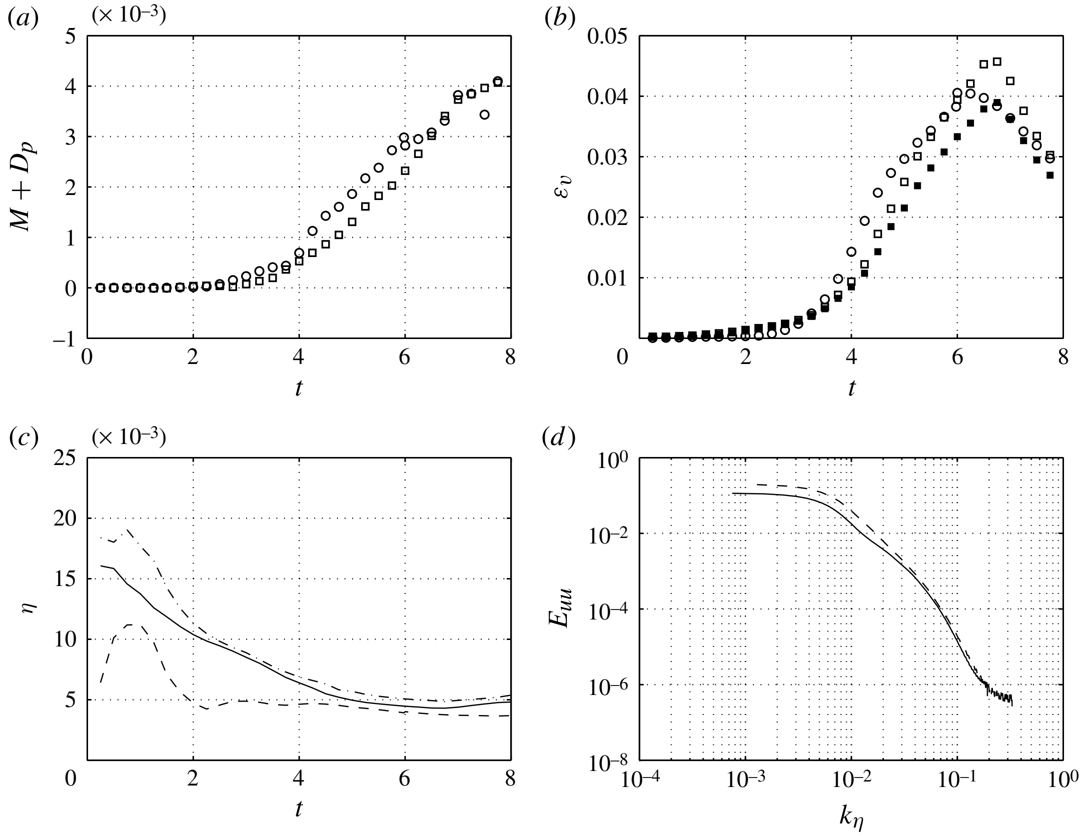

FIGURE 18. Comparison between ILES and DNS ($Re = 4000$) for $\gamma = 042$. (*a*) Irreversible mixing for ILES (circles) and DNS (squares). (*b*) Viscous dissipation for ILES (open circles) and DNS (open squares, KE residual; closed squares, explicit dissipation). (*c*) Kolmogorov microscale for ILES (dashed) and DNS (solid, based on explicit dissipation; chain-dotted, based on residual dissipation). (*d*) One-dimensional ($x-$) energy spectrum for the u velocity component for ILES (dashed) and DNS (solid), $t = 6$.

grid resolution is $\sim 1.5\eta$ for the minimum value of η, a higher resolution than accepted standards for accurate DNS (Moin & Mahesh 1998, §2.1). In addition, it can be seen that in the DNS the two estimates for η, based on the resolved and residual dissipation, agree very well, lending further support that the dissipation scales are resolved. As a final point, note that in the ILES, η is initially smaller than for the DNS. Because the Kolmogorov scale is set by the grid resolution, the effective Reynolds number for ILES is initially higher, then decreases as turbulence develops. This permits the development of smaller scales earlier in the flow, which can be seen by comparing the ILES in figure 2(*c*) with the DNS in figure 17.

Figure 18(*d*) compares turbulent energy spectra for ILES and DNS. These are calculated from the $1 - D$ streamwise ($x-$) spectrum of the $x-$ component of velocity, averaged in the middle part of the domain, from $-1 < y < 1$ to $0.35 < z < 0.65$ at $t = 6$ (wavenumber is normalized by η at the corresponding time). While there are some differences at large wavenumber, presumably due to subtle differences in the temporal evolution, the high-wavenumber behaviour is almost identical. The DNS is resolved well into the dissipation range $k\eta \gtrsim 0.1$, and is tracked almost identically by the ILES spectrum up until its Nyquist cutoff at $\kappa\eta \approx 0.33$. This suggests the energy transfer to the dissipation range is well-captured by ILES (for a *Re* equivalent to the DNS). We emphasize that this particular value of γ represents perhaps the most stringent test of the dissipation-range behaviour of ILES.

9. Discussion: comparison with the Haro Strait observations of Farmer *et al.*

The original motivation for this investigation was Farmer *et al.* (2002) who observed shear flows behind Stuart Island in the Haro Strait with $\Delta U \approx 2$ m s^{-1}, $l_u \approx 50$ m and a horizontal $\Delta\rho/\rho_o \approx 5 \times 10^{-4}$ in water approximately 200 m deep. These give $\gamma \approx 0.6$ and is in the regime where shear instability and lateral buoyancy adjustment evolve on similar time scales. Based on the numerical results presented here (cf. figure 8), we would expect a surface vortex with a width of the order of the depth. Farmer *et al.* (2002) observed an eddy with radius of order 100 m, consistent with the numerical results. For similar γ, we found vertical currents of order $(g'H)^{1/2}$, which for the Haro Strait parameters would correspond to $w \approx 1$ m s^{-1}. This estimate from the model is consistent with the observed vertical currents up to 0.5 m s^{-1}.

Farmer *et al.* did not make direct measurements of the density field within the tilted interfacial zone, but their observations of the velocity field showed that the shear layer had broadened from $l_u \approx 50$ m at the separation point to $l_u \approx 300$–500 m at the second observation section 4.5 km downstream. The mean velocity of the shear layer $U_o \approx 1$ m s^{-1}, giving a time scale $\tau = 4500$ s for the advection between the observation sections. This advection time and interface thickness growth imply a horizontal diffusivity $K_{obs} \sim l_u^2/\tau = 20$–55 m^2 s^{-1}. For the $\gamma \approx 0.6$ range of the field experiments, the numerical results do not show a diffusive behaviour. However, using our numerical result from the $\gamma = 0.21$ case as a rough estimate, would give $\hat{K} \approx 60$ m^2 s^{-1} in dimensional units based on the time scale $(H/g')^{1/2}$ and $H = 200$ m. This estimate is of the same order as the observational estimate and certainly encouraging, but some caution is warranted because of the dependence of mixing on γ and also, as we find, on l_u (although the field value of $l_u/H \approx 1/4$ is comparable to our $l_u = 1/6$ runs).

The numerical results are broadly consistent with the Farmer *et al.* observations and their explanation of shear-layer evolution by vortex stretching and tilting. However, we have also identified a secondary shear-layer instability at the surface caused by frontal convergence and shear intensification, which Farmer *et al.* did not report. Their qualitative model of the vorticity generation envisioned a continuous stretching of the primary shear vortex by the gravitational adjustment as it was swept downstream. The present numerical results suggest that both stretching and tilting of the primary vortex intensify the vorticity, but this process is later interrupted by rapid dislocation of the primary cores. Vortex tilting then generates a vertical overturning circulation, which is strengthened through the interaction with Kelvin–Helmholtz vortices associated with the gravity current collapse and the conversion of the vertical vorticity to horizontal vorticity. This overturning is responsible for the mixing observed in the simulations, and likely also in the field observations.

There are two important differences between our simulations and the field observations. First, we study the temporal growth in a spatially periodic shear layer, whereas the Haro Strait flow is a spatially growing mixing layer. This could introduce subtle differences in the development, such as coupling between adjacent Rayleigh vortices. Second, in the Haro Strait, the slow- and fast-moving streams have vertical stable stratification in addition to the horizontal density gradient. This vertical stratification could partially restrict overturning and vertical mixing.

10. Conclusions

We have presented results on flows with horizontal shear and horizontal density gradients. These share common features with pure shear flows and gravity currents, but are more complex due to interactions between the turbulent features of each. The tilting of vertical vorticity produced by the horizontal shear results in vertical overturning circulation. Shear intensification at frontal convergences produces high-wavenumber, intensified vertical vorticity. Transverse Kelvin–Helmholtz vortices associated with the gravitational adjustment interact with the tilted vortices to produce vertical mixing. The details of these interactions, and the rate at which turbulence develops, depend upon the relative time scales of shear instability and gravitational adjustment, described by the parameter γ.

For $\gamma \approx 1$, in the gravity-current-dominated regime a secondary instability associated with frontal convergence was identified. The convergence enhances the cross-front shear, producing high-wavenumber vertical vorticity that leads to three-dimensional turbulence. The three-dimensional instability is similar in appearance to the lobe–cleft instability observed in classical gravity currents over no-slip boundaries, but has a very different generation mechanism. Through this secondary instability, a relatively small amount of horizontal shear is sufficient to promote a transition to three-dimensional turbulence and increase mixing. However, for $\gamma \gtrsim 0.83$ the gravity current front propagates with constant speed, as in a traditional gravity current.

For $\gamma \lesssim 0.6$, the influence of horizontal shear becomes even more significant. The initial development of the horizontal shear instability is rapid, producing well-developed vertical vortex cores. By analysing the vorticity production, we find that both stretching and tilting of these vortices is important to subsequent flow development. Near the surface and bottom fronts, vortex stretching concentrates vertical vorticity, enhancing it by an order of magnitude. The tilting of these primary vortices converts vertical to horizontal vorticity and produces vertical overturning. The overturning results in strong downwelling vertical currents at the surface front. The combination of gravitational collapse, vortex tilting and stretching, and the secondary shear instabilities results in rapid breakdown of the flow and turbulent mixing.

An analysis of the energy budgets shows the transition from gravity current to mixing layer behaviour as γ is reduced. For large γ, potential energy is converted into kinetic energy through the buoyancy flux. There is relatively little irreversible mixing. In the shear-dominated regime, the dominant energy exchange is between the available and background potential energy reservoirs, as mixing increases the latter at the expense of the former. In this strong-mixing regime, the total potential energy remains relatively constant and the kinetic energy is rapidly reduced by dissipation.

Mixing was investigated through the background potential energy, from which we defined an effective turbulent scalar diffusivity, proportional to the mean square growth rate of the mixed fluid thickness, $\hat{\sigma}$. For early times the mixed interface grows as $\hat{\sigma} \sim t^{5/2}$ for all γ. For smaller values of γ, there is a transition to diffusive scaling, $\hat{\sigma} \sim t^{1/2}$ as mixing slows the gravity current frontal propagation.

Acknowledgements

This research was supported by NSF Grant OCE-0726161. The numerical computations were performed at the National Center for Atmospheric Research under project number 35781072. We thank A. Almgren for access to IAMR.

REFERENCES

ALMGREN, A., BELL, J., COLELLA, P., HOWELL, L. & WELCOME, M. 1998 A conservative adaptive projection method for the variable density incompressible Navier–Stokes equations. *J. Comput. Phys.* **142**, 1–46.

ASPDEN, A., NIKIFORAKIS, N., DALZIEL, S. & BELL, J. B. 2008 Analysis of implicit les methods. *Comm. App. Math. Com. Sc.* **3** (1), 103–126.

BASAK, S. & SARKAR, S. 2006 Dynamics of a stratified shear layer with horizontal shear. *J. Fluid Mech.* **568**, 19–54.

BENJAMIN, T. 1968 Gravity currents and related phenomena. *J. Fluid Mech.* **31**, 209–248.

BOCCALETTI, G., FERRARI, R. & FOX-KEMPER, B. 2007 Mixed layer instabilities and restratification. *J. Phys. Oceanogr.* **37** (9), 2228–2250.

BOULANGER, N., MEUNIER, P. & DIZÈS, S. L. 2008 Tilt-induced instability of a stratified vortex. *J. Fluid Mech.* **596**, 1–20.

BROWN, G. & ROSHKO, A. 1974 On density effects and large structure in turbulent mixing layers. *J. Fluid Mech.* **64**, 775–816.

CARPENTER, J. R., BALMFORTH, N. J. & LAWRENCE, G. A. 2010 Identifying unstable modes in stratified shear layers. *Phys. Fluids* **22** (5), 054104.

CORCOS, G. & LIN, S. 1984 The mixing layer - deterministic models of a turbulent-flow 2. The origin of the 3-dimensional motion. *J. Fluid Mech.* **139** (FEB), 67–95.

FARMER, D., PAWLOWICZ, R. & JIANG, R. 2002 Tilting separation flows: a mechanism for intense vertical mixing in the coastal ocean. *Dyn. Atmos. Oceans.* **36** (1–3), 43–58.

HARTEL, C., CARLSSON, F. & THUNBLOM, M. 2000*a* Analysis and direct numerical simulation of the flow at a gravity-current head. Part 2. the lobe-and-cleft instability. *J. Fluid Mech.* **418**, 213–229.

HARTEL, C., MEIBURG, E. & NECKER, F. 2000*b* Analysis and direct numerical simulation of the flow at a gravity-current head. Part 1. flow topology and front speed for slip and no-slip boundaries. *J. Fluid Mech.* **418**, 189–212.

HUERRE, P. 1983 Finite amplitude evolution of mixing layers in the presence of solid boundaries. *J. de Méc. Théor. Appl.* 121–145.

IVEY, G. N., WINTERS, K. B. & KOSEFF, J. R. 2008 Density stratification, turbulence, but how much mixing?. *Annu. Rev. Fluid Mech.* **40**, 169–184.

LASHERAS, J. & CHOI, H. 1988 3-dimensional instability of a plane free shear-layer - an experimental-study of the formation and evolution of streamwise vortices. *J. Fluid Mech.* **189**, 53–&.

LAWRIE, A. & DALZIEL, S. 2011*a* Turbulent diffusion in tall tubes. I. Models for Rayleigh–Taylor instability. *Phys. Fluids* **23**, 085109 DOI: 10.1063/1.3614477.

LAWRIE, A. & DALZIEL, S. 2011*b* Turbulent diffusion in tall tubes. II. Confinement by stratification. *Phys. Fluids* **23**, 085109 DOI: 10.1063/1.3622770.

LINDEN, P. & SIMPSON, J. 1986 Gravity-driven flows in a turbulent fluid. *J. Fluid Mech.* **172**, 481–497.

MARGOLIN, L. G., SMOLARKIEWICZ, P. K. & WYSZOGRADZKI, A. A. 2006 Dissipation in implicit turbulence models: a computational study. *J. Appl. Mech.* **73** (3), 469–473.

MICHALKE, A. 1964 On the inviscid instability of the hyperbolic tangent velocity profile. *J. Fluid Mech.* **19** (4), 543–556.

MOIN, P. & MAHESH, K. 1998 Direct numerical simulation: a tool in turbulence research. *Annu. Rev. Fluid Mech.* **30**, 539–578.

MONISMITH, S., KIMMERER, W., BURAU, J. & STACEY, M. 2002 Structure and flow-induced variability of the subtidal salinity field in northern San Francisco Bay. *J. Phys. Oceanography* **32** (11), 3003–3019.

PELTIER, W. & CAULFIELD, C. 2003 Mixing efficiency in stratified shear flows. *Annu. Rev. Fluid Mech.* **35**, 135–167.

PIERREHUMBERT, R. & WIDNALL, S. 1982 The two- and three-dimensional instabilities of a spatially periodic shear layer. *J. Fluid Mech.* **114**, 59–82.

PIOTROWSKI, Z., SMOLARKIEWICZ, P., MALINOWSKI, S. & WYSZOGRODZKI, A. 2009 On numerical realizability of thermal convection. *J. Comput. Phys.* **228**, 6268–6290.

SHIH, L., KOSEFF, J., IVEY, G. & FERZIGER, J. 2005 Parameterization of turbulent fluxes and scales using homogeneous sheared stably stratified turbulence simulations. *J. Fluid Mech.* **525**, 193–214.

SIMPSON, J. E. 1999 *Gravity Currents: In the Environment and the Laboratory*, 2nd edn. Cambridge University Press.

WAITE, M. & SMOLARKIEWICZ, P. 2008 Instability and breakdown of a vertical vortex pair in a strongly stratified fluid. *J. Fluid Mech.* **606**, 239–273.

WINANT, C. & BROWAND, F. 1974 Vortex pairing, the mechanism of turbulent mixing-layer growth at moderate Reynolds number. *J. Fluid Mech.* **63**, 237–255.

WINTERS, K., LOMBARD, P., RILEY, J. & D'ASARO, E. 1995 Available potential energy and mixing in density-stratified fluids. *J. Fluid Mech.*.

YOUNG, W. 1994 The subinertial mixed-layer approximation. *J. Phys. Oceanogr.* **24** (8), 1812–1826.